THE JOURNAL OF
PHYSICAL CHEMISTRY C

ARTICLE

pubs.acs.org/JPCC

The Role of Oxygen during Thermal Reduction of Graphene Oxide Studied by Infrared Absorption Spectroscopy

Muge Acik,[†] Geunsik Lee,[†] Cecilia Mattevi,[‡,§] Adam Pirkle,[†] Robert M. Wallace,[†] Manish Chhowalla,[‡] Kyeongjae Cho,[†] and Yves Chabal*,[†]

[†]Department of Materials Science and Engineering, University of Texas at Dallas, Richardson, Texas 75080, United States

[‡]Materials Science and Engineering, Rutgers University, Piscataway, New Jersey 08854, United States

S *Supporting Information*

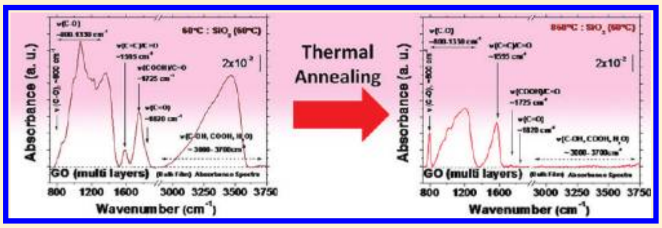

ABSTRACT: Understanding the thermal reduction of graphene oxide (GO) is important for graphene exfoliation, and chemical and morphological modifications. In this process, the role of trapped water and the evolution of oxygen during annealing are still not well-understood. To unravel the complex mechanisms leading to the removal of oxygen in reduced GO, we have performed in situ transmission infrared absorption spectroscopy measurements of GO films upon thermal annealing at 60−850 °C in vacuum (10^{-3}−10^{-4} Torr). Using cluster-based first-principles calculations, epoxides, ethers (pyrans and furans), hydroxyls, carboxyls, lactols, and various types of ketones and their possible derivatives have been identified from the spectroscopic data. Furthermore, the interactions between randomly arranged nearby oxygen species are found to affect the spectral response (red and blue shifts) and the overall chemistry during annealing. For instance, the initial composition of oxygen species (relative amounts and types of species, such as hydroxyls, carboxyls, and carbonyls) and reduction times determine the final oxygen concentration (% of initial concentrations), varying from ∼46−92% in multilayer GO to ∼3−5% in single-layer GO. In the multilayer case, there is no dependence on the layer thickness. An important indicator of the reduction efficiency is the relative concentration of carbonyls at intermediate annealing temperatures (∼200 °C). These observations suggest that thermal annealing can foster the formation of free radicals containing oxygen in the presence of trapped water in GO, which further attack carboxyls, hydroxyls, and carbonyls, preferentially at edges rather than on basal plane defects. These findings impact the fabrication of electronics and energy storage devices.

1. INTRODUCTION

Carbon is abundant in organic compounds that form the basis of life as well as in mineral forms from which several functional materials are derived. Among organic compounds, the chemistry of aromatic and heterocyclic groups has been intensively investigated for their broad use in polymer industry, fuel refining, and in biochemistry due to their presence in amino acids and nucleotides.[1] Therefore, an understanding of the chemical reactivity of aromatic compounds is of wide interest. In addition, the chemistry of aromatic and heterocyclic compounds can also be used to understand the chemical properties of other forms of sp^2 carbons, such as monolayer membranes of conjugated carbons that are extensively used in large area and molecular electronics.[2] The most prominent example of such a material is graphene. It is a single layer of graphite that has superlative electrical, mechanical, and chemical properties, which make it unique for development of future nanotechnology. Consequently, practical routes to efficiently extract graphene from intercalated graphite[3] via exfoliation into the individual layers of graphene have been actively sought. In this context, graphite oxide (∼C_8O_2H), a compound where different oxygen functionalities are covalently bound to the carbon atoms within the hexagonal basal plane, has garnered significant attention because it leads to the isolation of individual layers of chemically functionalized graphene via an inexpensive, low-temperature, and easily controllable one-step process of oxidation and exfoliation in aqueous solution. The oxygen content in individual layers of chemically functionalized graphene can then be tailored by further thermal or chemical processes, leading to different optoelectronic, mechanical, and chemical properties. Because of the variety of oxygen functionalities that can be present either within the carbon basal plane or at the edges of an individual layer of chemically derived graphene and their rapid transformation by applying slight variations in the environment, graphene oxide represents a model system for understanding the carbon−oxygen interplay in aromatic structures. It is, therefore, important to monitor the carbon−oxygen bond evolution in chemically derived graphene as a function of temperature and interlayer interaction between several oxidized graphene layers.

Received: June 4, 2011
Revised: August 10, 2011
Published: September 16, 2011

dx.doi.org/10.1021/jp2052618 | J. Phys. Chem. C 2011, 115, 19761–19781

Graphene oxide (GO), first discovered in 1859 by Brodie[4] and further modified by Staudenmaier,[5] Hummers, and Offeman,[6] has turbostratic random ordering with 6-fold symmetry of stacking[7] and an interlayer spacing of 0.625 nm when fully oxidized.[8] Intercalation of water between layers (interlayer spacing ranging from 6.4 to 11.3 Å depending on the amount of water)[9] is possible due to the hygroscopic nature of GO.[10] GO is the most promising modified graphene precursor for large-scale production (commercial scalability) and for functionalization to derive graphene-like structures with controllable electronic, optoelectronic, mechanical, and transport properties. It can readily be deposited on a variety of substrates.

Control of GO stoichiometry is, however, difficult. The initial oxygen concentration depends critically on processing, and the reduction pathways are not well-understood.[11] Reasons for variations in the functional group density involve variation of its elemental composition depending on the nature of the pristine graphite, its particle size, oxidizing reagents, oxidation level, synthesis method,[12] and, more importantly, the oxidation time.[13] For instance, an increase of the oxidation time results in a high conversion of hydroxyls to epoxides, as shown by Jeong et al.[7] Many models are, therefore, possible due to the non-stoichiometry and diverse composition of GO,[11] as proposed by Lerf,[14] Gao,[15] Fuente,[16] and Jeyong.[17]

Experimental studies have mostly focused on the identification of nucleophilic sites, such as hydroxyls, small amounts of carboxyls and carbonyls,[11,18] epoxides, 1,3-epoxy bridges, C=C,[19] armchair edges, semiquinone and basal epoxy groups,[20] tertiary C−OH groups,[12] quinone, furan-like bridges, and five-membered lactones.[21] Similarly, first-principles calculations have provided relevant information for the presence of ethers (more stable than epoxide groups), in the process of oxidation due to structural bistability,[22] peroxides, 1,4 ethers (rare and not dominant), and vacancy defects (one or two missing atoms, including reactive dangling bonds).[23] Among the above structures, the position of oxygen in ether-like structures is the least known. It can be in the form of either 1,2-ether or 1,3-ether. It was also suggested that there are hydroxyls and ether-like oxygen bridges between one and three carbon atoms with random distribution.[24]

Infrared absorption spectroscopy is an important tool for characterization of these functional groups[25,26] and has shown that the edges of GO are likely to have pyrone-like functionalities (basic surface oxides). These groups include both sp^2- and sp^3-hybridized oxygen atoms, which vary based on the pK_a values of the various possible combinations of different ketone and ether-like rings. Other infrared spectroscopic studies have focused on functionalized GO,[27] GO papers,[28] and GO nanoplatelets[29] using diffuse reflectance, although issues remain in the peak assignments. At higher annealing temperatures (∼850 °C), only ethers arranged in atomically straight lines appear to be stable.[30]

Recently, NMR studies have shown the presence of five- and six-membered-ring lactols, 2-hydroxynaphthalic anhydrides, and 1,3-dihydroxyxanthones using solid-state ^{13}C magic-angle spinning (MAS) NMR.[15] Other functionalities have also been reported, such as quinone, furan-like bridges, five-membered lactones,[31] as well as the existence of enol groups.[32] Moreover, hydroxyl groups adjacent to C=C bonds (namely, enol groups) have been shown to be in equilibrium with keto forms.[33]

In all these studies, the interactions between functional groups have been ignored. Yet, interactions of adjoining oxygen groups are likely to occur depending on their spatial arrangements.[34] So far, there is some evidence from XPS studies that epoxy, hydroxyl, and lactol groups are located nearby,[14] which has also been confirmed with ^{13}C NMR magic-angle spinning (MAS),[35] ^{13}C and ^{1}H NMR,[14] solid-state (SS) NMR with ^{13}C-labeled GO,[36] and solid-state ^{13}C magic-angle spinning NMR.[15] Similarly, a quantum chemical study of activated carbons has suggested that a red shift of C=O frequencies should occur in the presence of neighboring hydroxyl groups.[16]

Studies have also focused on determining the extent of oxygen removal and exfoliation of GO, since chemical[37] and thermal reduction[38] of graphene (or graphite) oxide are promising routes toward isolating graphene layers from bulk graphite for large-scale production. For instance, a recent Fourier transform infrared (FTIR) study of thermally reduced GO after 200 °C in argon ambient could identify the removal of water, hydroxyl, epoxide, and carboxyl groups.[39] Elemental analysis showed that the C/O ratio increased from 2:1 in graphite oxide to 10:1 in reduced GO upon thermal treatment,[40] and 27% of oxygen is removed upon heating to 180 °C and a further 10% at above 180 °C.[41]

There have not, however, been systematic studies to characterize the detailed structural composition of GO and to investigate both the chemical and the thermal reduction mechanisms of GO. This is, in part, due to the dearth of in situ studies, but also in the difficulties associated with data analysis for a system that is characterized by random arrangement of oxygen. For instance, a major difficulty for infrared spectroscopy, typically used to identify gas-phase molecules,[42] is the assignment of modes that involve several adjacent configurations and are, therefore, very different from isolated chemical groups (with well-documented vibrational frequencies). To make progress, it is important to investigate and take into account the effects of interactions between randomly arranged oxygen functionalities. For this reason, we combine infrared absorption measurements with theoretically simulated infrared frequencies and intensities (strength of each vibrational mode) using density functional theory (DFT) calculations. Thus, we are able to provide a more realistic interpretation of observed spectra using a number of cluster models featuring several different arrangements of oxygen functionalities expected to occur during the thermal annealing process. Using both qualitative spectral analysis and quantitative estimation of oxygen concentrations, we are able to provide useful insight into possible thermal reduction mechanisms.

2. BACKGROUND AND MOTIVATION FOR MODELING AND QUANTIFYING OXYGEN FUNCTIONALITIES IN GO

2.1. Modeling Issues (Structural Evolution of Oxygen Functional Groups). A detailed understanding of the chemical structure of graphite oxide and reduced graphene oxide sheets is complicated by a potential dependence on the processing agreement. The present effort employs simple reduction schemes that permit basic structural derivation of GO with commonly known oxygen groups. However, the degree to which the chemical properties of the reduced graphene oxide sheets vary with the reduction protocol, therefore, needs to be carefully explored.

The structural evolution of oxygen groups in GO has been only partially studied. For instance, it is known that GO consists of pentagonal and hexagonal systems that have aromatic regions with nonoxidized benzene rings and regions with aliphatic six-membered rings.[14] It is also known that isolated hexagons of carbon atoms extruding from armchair edges have also been observed when the straight edge is partially broken.[43] Recently, five- and six-membered-ring lactols at the edges have also been reported by Gao et al. based on interpretation of NMR data, suggesting that these groups are responsible for oxygen-containing impurities.[15] However, these lactols may only be minority species. One of the DFT calculations also confirms that functionalization by both oxygen and hydroxyl is more favorable than by hydroxyl groups only.[44]

Other important intermediate species in the formation of GO are carbonyls, epoxides, hydroxyls, and ether groups. Carbonyls at the edges are either isolated or arranged in a quinone-like fashion, two neighboring carbonyl groups that represent the most stable oxygen configuration, as suggested in ref 34. Studies also show that oxygen functionalities of GO, for example, enolic groups (with hydroxyl neighbor) and another adjacent carboxyl group, are stabilized by inducing repulsive forces, such as electrostatic stabilization between negatively charged carboxylate groups[45] at the edges of graphene sheets.[46] Such functional groups influence the selective molecular intercalation or the adsorption of ions and molecules, leading to a variety of covalent modifications.[47] On the basal plane, out-of-plane groups, such as epoxides and hydroxyls, are present, although much less stable. Epoxides are typically present at a lower concentration in comparison to hydroxyls.[48] Oxygen in the form of ether (either xanthene or pyran) is difficult to detect by most techniques and has, therefore, not been discussed as much. Although these issues have been already recognized, there is still a lack of experimental evidence necessary to identify all these functionalities, and clarify the interaction mechanisms, in particular, the role of oxygen during GO reduction.

On the basis of the factors summarized above, we have designed simple cluster models for the most plausible oxygen groups, as motivated by the model structures presented in refs 44 and 34, and determined the associated vibrational modes and frequencies by DFT calculations.

2.2. Issues with Spectral Interpretations. IR spectroscopy is a powerful tool to unravel the composition and evolution of graphene/graphite oxide. This technique is complementary to either ^{13}C or ^{1}H NMR or XPS analysis. So far, IR analysis has been performed mostly for evaluating the spectral changes either at room temperature or after chemical or thermal reduction. Previous IR studies have been interpreted on the basis of simple model molecules using common infrared tables. In general, conjugation and proximity effects can lead to substantial frequency shifts and need to be taken into account, which has not been the case so far. Consequently, determination of GO chemical composition has been difficult.

For instance, the identification of ketone and carboxyl groups is difficult, and are mostly referred to as "carbonyls" (e.g., an intense peak at 1732 cm^{-1} was ascribed to the stretching vibration of a carbonyl by Melucci et al.)[49] or "C=O group" (at 1750 cm^{-1} by Nakajima et al.).[50] Although Chen et al.[51] assigned a peak at 1734 cm^{-1} to carbonyls, they were not able to identify whether it was a carboxyl or a ketone. The overlapping spectral features in the 1650−1850 cm^{-1} region complicate the spectral interpretations of as-synthesized GO. Therefore, it is impossible to distinguish these infrared modes without using further differentiation methods (e.g., selective removal of some species by thermal annealing). This difficulty has led to confusing assignments. For example, absorption bands at 1630 cm^{-1} for GO and 1570 cm^{-1} for reduced GO (rGO) were attributed to the asymmetric vibrations of the carboxylate groups,[52] partly because the contribution from ketones in this region could not be distinguished. Taking into account the shifts associated with π-conjugation in benzene rings, the peaks at 1700[53] and 1730[54] cm^{-1} were both attributed to the carboxyl groups adjacent to benzene groups. Indeed, Shen et al. reported a lower frequency at 1650 cm^{-1} for noninteracting carboxyl groups.[55] Furthermore, the deformation mode of the C−O band of a carboxyl was first associated with a peak observed at 1100 cm^{-1} in a thermal annealing study monitored by thermal gravimetric analysis (TGA).[56] Another tentative assignment of a peak at 1647 cm^{-1} to carboxyl was made for the nonoxidized graphitic domains by Kim et al.[57]

The presence of the other species, such as stretching and bending modes of hydroxyls and ethers, also complicates the identification of carboxyls and ketones in lower-frequency spectral regions (800−1500 cm^{-1}). Absorption features at 1414 cm^{-1} (carboxy)[58] or 1410 cm^{-1} have mostly been assigned to the deformation vibrations of C−OH groups,[37] an assignment that ignores the contribution of ketones in this frequency region. Lee et al. were the first to assign a peak at 1680 cm^{-1} to the vibrational mode of the ketone groups. However, they were not able to interpret the peaks below 900 cm^{-1}. Similarly, the assignment of modes at 1705, 1730, and 1750 cm^{-1} to free carboxyls, esters, and lactone groups, respectively, has been made for carbon fibers.[59] The assignment of the weak vibrational modes in the bending mode region for hydroxyls and carboxyls at lower frequencies has also been difficult. For instance, Yan et al.[60] have assigned the peak at 1365 cm^{-1} to a C−OH, while assigning only one peak to both carboxylic acid and carbonyl moieties at 1732 cm^{-1}. In other studies, the stretching modes of carboxyl groups were ignored and only a weak absorption at 1356 cm^{-1} was assigned to the stretching vibrations of carboxyls.[61] Nonetheless, only IR measurements are sensitive enough to determine the presence of carbonyl groups despite potentially controversial assignments. NMR studies have not been able to confirm the existence of carboxyl groups due to difficulty in differentiation of the overlapping binding energies.[62]

Similarly, epoxies have been identified, but the assignment of their associated vibrational modes has been unclear in most cases. Only one or two modes of the ether groups have been assigned. Some studies have avoided the 800−1330 cm^{-1} spectral region altogether because of the overlap of hydroxyl and carboxyl frequencies. Indeed, contributions in the 1000−1180 cm^{-1} region may arise from hydroxyls, carboxyls, ethers, epoxides, and ketones. A mode at 1057 cm^{-1} was attributed to a C−O in C−OH or C−O−C functional groups by Xu et al.,[63] an assignment that ignores possible weak contributions from carboxyls and ketones. Absorption bands at 1220, 880, and 850 cm^{-1} have been assigned to the symmetric stretching, asymmetric stretching, and deformation vibrations of epoxy groups, respectively.[64] However, the band at 1220 cm^{-1} may also originate from a ketone, instead of an epoxy. In other studies, the C−OH stretch mode was placed at 1226 cm^{-1},[65] where ketone also has a weak contribution (see Table 2). Gonc et al. assigned the two modes at 1139 and 873 cm^{-1} to C−O in epoxy groups. However, they were not able to distinguish scissor modes of water and ketone from aromatic carbon double bonds, all occurring at ~1620 cm^{-1},[66] whereas Bon et al. interpreted a similar absorption to vibrations of nonoxidized graphitic domains.[67] In general, the identification of sp^2-hybridized C═C groups at 1580−1600 cm^{-1} is also greatly complicated by the scissor mode of water (deformation vibration) at 1630−1650 cm^{-1}.

Another challenge has been the identification of C−O stretch modes of CO and CO_2 in the 2200−3000 cm^{-1} region that overlaps within a broad feature with C−OH stretch modes (2800−3600 cm^{-1}), arising from a number of functionalities (e.g., tertiary alcohols, enols, phenols, and COOH)[46] involved in hydrogen-bonding interactions with widely varying strengths. In the work of Pham et al.,[68] for instance, the observation of modes at 1703 and 3188 cm^{-1} was used to identify carboxylic groups, but additional contribution in the O−H stretch region was not taken into account. Indeed, other studies have observed and assigned bands at 3616 and 3490 cm^{-1} to hydroxyl species.[69] Hontoria-Lucas et al.[70] first identified a broad band at 3000−3700 cm^{-1} showing two maxima at around 3190 and 3403 cm^{-1} and a shoulder at approximately 3590 cm^{-1}. These were attributed to the presence of the free and associated hydroxyl groups, due to "adsorbed and inhibited" water molecules and to the hydroxyl groups of GO. In this study, therefore, we clarify the spectral interpretations using a stepwise thermal reduction protocol, where we can differentiate each functional group with matching the simulated frequencies.

2.3. Issues in Identifying Thermal Reduction Mechanisms. Apart from the challenges discussed above regarding the vibrational mode assignments in the infrared studies, a major challenge remains with describing the evolution of functional groups and deriving the mechanisms of thermal reduction. Such an understanding is important because the physical properties are dramatically modified upon reduction. For instance, electrical current−voltage ($I-V$) measurements of the thermally reduced GO at moderate temperatures (100−250 °C) leads to large band-gap variations in graphene oxide.[71] Furthermore, Jung et al. demonstrated a significant increase in the electrical conductivity when heated in vacuum at 125−240 °C, which is consistent with partial reduction of GO.[72] In general, thermal reduction studies have been performed for a relatively narrow temperature range and there have been no stepwise annealing studies, which makes it difficult to develop a full picture of the reduction process. The situation is even more complex when attempting to determine the exact temperature regimes at which each oxygen group is removed. For instance, pyrones are known to be quite heat-resistant from studies with oxidized carbon blacks, which are desorbed in the form of CO and CO_2 only between 800 and 950 °C.[73] In contrast, other studies suggest that carboxyls were removed, but the carbonyls remained even after annealing at 1000 °C.[74]

The hydroxyls attached to the interior of an aromatic domain are easier to remove than those at the edges of the aromatic domain. These hydroxyl groups are eliminated at temperatures higher than approximately 700 °C.[74] Although such assumptions are made using both experimental and theoretical studies, the mechanisms of thermal reduction are not yet well-understood and clarified.

2.4. The Role of Hydroxyl Radicals during Thermal Reduction. In principle, hydroxyl radicals are also likely to be produced from reactions of the zigzag edge graphene with an attack of water onto the carbon dangling sites, which occur much more readily than that of the armchair edge graphene.[75] Therefore, another challenge is the presence of water, which offers a possible alternative source for hydroxyl radical production with the help of abundant electrons of dangling bonds in the π-conjugated carbon network in addition to the other possible species, such as O_2, H_2O, and H_2O_2, which further catalyze the reactions. Having all these species in a medium, the residual oxygenated functional groups in the reduced GO are found to be capable of facilitating desorption/ionization processes[76] (deprotonation of carboxyls, enols, and phenolic groups following protonation of ether and carbonyl groups) or radical cations,[77] in the presence of analytes, which still requires further understanding. In general, trapped water offers control of radical reactions,[78] though high reactivity of the hydroxyl radicals as oxidants brings uncertainities to explain these reactions.

Little attention has been paid to these radicals so the radical reactions in water remain to be studied. Indeed, derivation of a reaction pathway for the radicals is difficult because free radicals are active species. Therefore, it is crucial to examine hydroxyl radicals and their function in various ionization processes because OH radicals are able to attack carbon atoms with a dangling bond, as shown already for SWNTs.[79] Carbons also react with the free radicals (mostly peroxides), which also further attack other radical sites.[80] Similarly, radicals are formed due to a partial oxidation reaction during growth of metal template encapsulating graphite or oxidation of ethylene.[81] Meanwhile, many different carbon-containing radicals are also formed as a function of temperature. These carbon radicals adsorbed on the surface decompose[82] and lead to the reactions with dangling bonds at the graphene edges with new radicals (minimum free energy configuration).[83] For example, catalytic etching of ethylene requires hydroperoxide radicals (HO_2) during oxidation at 775−925 K.[84] Therefore, hydroxyl radicals are capable of generating new oxygen-containing species in the presence of a catalytic environment and further oxidizing the carbon backbone.

2.5. Defect Formation. Defects, in principle, serve as the binding sites for chemisorption and radical formation, especially hydroxyl radicals in the presence of thermally dissociated water.[85] The production and the release of CO and CO_2 is a result of a thermally induced oxidative disruption[86] of the GO lattice, leading to random locations in the film.[87] However, the chemical reaction pathways for production of CO and qCO_2 involved in the thermal reduction process are not well-characterized so far. However, CO is a strong reducing agent, so it is possible that much of the CO_2 production occurs via multistep processes. One proposal is that oxygen can transform to O_2 from reactions with OH radicals and the secondary reactions with H_2O_2. OH radicals are then further likely to react with CO and form CO_2 or COOH radicals. With increasing temperature, these radicals tend to decompose, leading to faster CO_2 formation.

Similarly, the mechanism for the formation of CO is not well-explained. There are plausible approaches deriving from combustion reactions. For instance, CO_2 can react with the carbon surface to give CO, which further reacts with the surface oxygen complexes to give CO_2 at lower temperatures, and then decomposes at 250 °C. Alternatively, zigzag graphene edges constitute active carbon sites with negative charges and can form oxygen complexes with different levels of stability.[88] Therefore, O_2 can be one of the main sources for the formation of CO/CO_2 with reactions at these carbon active sites triggered by radical species.

In these intermediate temperature studies (200−350 °C), it was observed that CO reacts with hydroxyl radicals, forming CO_2. At temperatures below 200 °C, hydroxyl radicals are not completely converted to CO_2 with possible contributions from COOH and HCO radicals. At 200 °C, radicals attack CO (acting as a scavenger for hydroxyl radicals), forming a maxima for the CO_2 production. Thus, all these studies with different systems other than graphene motivate us to bring further spectroscopic evidence to understand the CO/CO_2 production and the associated defect formation.

3. EXPERIMENTAL METHODS

3.1. Synthesis and Preparation of GO. The starting material is commercially available graphite powder (SP-1 grade, 325 mesh, Bay Carbon Inc.). GO (multilayers) was obtained by oxidation of the graphite powder according to a modified Hummer's[89,90] method, including pretreatment using $K_2S_2O_8$ and P_2O_5 with careful temperature control. For purification, a prepared 2% w/w of aqueous GO dispersion with Milli-Q water was dialyzed for 2 weeks. This solution was used to deposit GO on clean SiO_2/Si substrates by drop-casting with a pasteur pipet. Prior to deposition, the substrate (Float Zone Si/SiO_2 (100), double-side polished) was mechanically cleaned by rubbing with a Q-tip soaked with ethyl acetate, ethanol, and distilled water and then chemically by immersion in a piranha solution, a mixture of H_2SO_4 and H_2O_2 (2:1, v/v) maintained at 90 °C for 15 min to remove all the organic residuals from the surface.

A controlled number of GO layers (e.g., 1 L, 3 L, and 5 L) could be prepared by controlling the GO concentration in solution and removing the cellulose filter membrane by dissolving it in acetone through a vacuum-filtration technique.[91] The thicknesses of GO thin films were determined by Raman scattering and tapping mode AFM, as reported in our previous work.[92] A GO monolayer exhibits a step height of about 1.0 nm. A single-layer GO film is obtained when a continuous coverage by individual monolayers is achieved. To achieve complete coverage, some overlap between GO sheets is necessary. Thus, the average film thickness is ∼1 nm for a single-layer film. Similarly, bilayered GO films have a step height of about 2.0 nm. Therefore, the argument can be extended to any n-layered GO films. The thickness measurements are highly reproducible, and the accuracy of the thickness determination is about ±0.25 layers. This variation can be attributed to the fact that the GO films are formed by individual flakes, which overlap in certain regions. The air-dried GO samples were then transferred onto clean hydrophilic silicon surfaces by either dissolution of membrane (namely, "GO-ML (thin)") or drop-casting (namely, "GO-ML (bulk)") for further FTIR analyses.

3.2. Analytical Instrumentation. Thermal annealing of GO samples on SiO_2/Si substrates was achieved by direct resistive heating of the Si substrates, using two tantalum clips in an evacuated chamber placed in an IR sample compartment of the spectrometer. The IR beam was incident on the surface close to the Brewster's angle (∼70°). The temperature was monitored by a K-type thermocouple spot-welded to a Ta clip attached to the sample edge. In this arrangement, the thermocouple readings are too low (∼20−50 °C) based on calibration of the thermocouple using a pyrometer. The errors are systematic so that the *relative* measurements are accurate and reproducible. The FTIR measurements were performed in a transmission geometry (typically 500 scans per loop), using a DTGS (deuterated triglycine sulfate) detector with a mirror optical velocity of 0.6329 cm/s at a resolution of 4 cm^{-1}. For in situ FTIR measurements, annealing was performed in the vacuum chamber and measurements were performed at 60 °C after each annealing sequence. The annealing time during a sequence was 5 min at each temperature for a stepwise reduction, and the total annealing time for the overall experiment per sample was approximately 18 h. Other possible reactions between the graphene oxide samples and the substrate native oxide (Si/SiO_2) are ruled out at high-temperature anneals (∼850 °C), as explained with details in ref 30. Analysis of each sample was repeated twice to assess the reproducibility and consistency of the IR data. An estimate of the total amount of oxygen is derived from the IR absorbance data, using the total integrated area of all the modes associated with oxygen functionalities. Such an estimate is only as accurate as the variation of the dynamic dipole moments of the various vibrational modes associated with each of the oxygen functionalities. Therefore, the relative amounts of oxygen quoted in this paper (atomic percent, referenced to the starting amount) have errors as large as a factor of 2, although the relative amount of specific functionalities is much more accurate (±10%).

3.3. X-ray Photoelectron Spectroscopy (XPS) Analysis. GO samples were characterized by XPS before and after reduction of GO. XPS spectra were collected using a monochromatic Al Kα X-ray source and Omicron EA 125 hemispherical analyzer. GO films were cast from solution onto Pt foils and reduced by furnace annealing (direct heating with a ramp rate of ∼10 °C/min) and the cast films at 900 °C (corresponding to ∼850 °C via current annealing) in vacuum (∼10^{-4} Torr) for 5 min (∼24 h of total annealing and cooling time).

3.4. Theoretical Method. First-principles density functional theory (DFT) calculations were carried out to investigate the possible interaction mechanisms. The vibrational frequencies were computed within a harmonic approximation by diagonalizing the dynamical matrix, consisting of the second derivative of the total energy with respect to atomic displacements. The total energy was computed using the Vienna Ab-initio Simulation Package (VASP)[93] with the projected augmented wave (PAW)[94] pseudopotentials for the electron−ion interaction and the local density approximation (LDA) for the exchange-correlation functional. The energy cutoff of 500 eV was used for the plane-wave basis expansion. Using periodic boundary conditions, a finite size cluster model was constructed to represent a specific oxidation group with the 10 Å vacuum region to decouple the interaction between periodic images and a 4 × 4 graphene supercell to introduce a vacancy defect. The criterion for structural optimization was that the total energy change between two ionic relaxation steps be smaller than 1 meV. Our DFT simulation predicts larger frequencies than the experimental values by 50 cm^{-1}, as verified by calculating the stretching mode of a gas CO (2220 cm^{-1} from our method, in comparison with the experimental value of 2170 cm^{-1}). In the tables, we report the simulated frequencies and corrected frequencies by subtracting 50 cm^{-1} from the simulated frequencies. The experimental frequencies are then compared with the corrected frequencies.

4. EXPERIMENTAL RESULTS

4.1. Spectral Assignments for GO at Room Temperature. To investigate the thermal evolution and interactions of

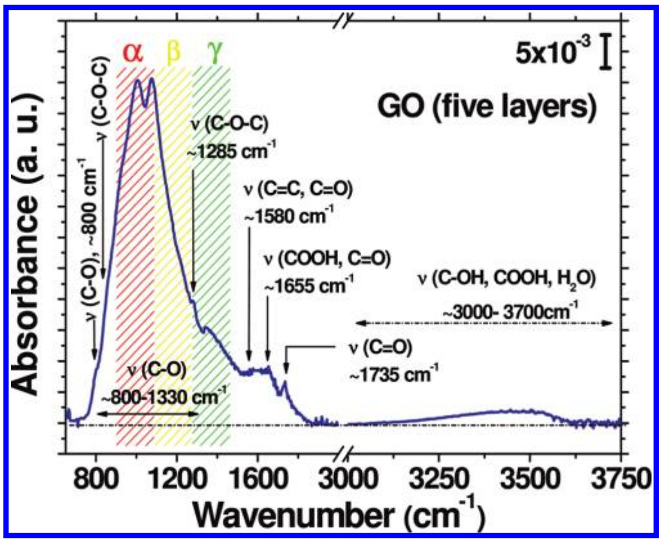

Figure 1. Transmission infrared absorbance spectrum of GO (five layers) at room temperature. Vibrational modes are shown for hydroxyls (possible COOH and H_2O contribution) (C−OH, 3000−3700 cm^{-1}), ketones (C═O, ~1750−1850 cm^{-1}), carboxyls (COOH and/or H_2O) (~1600−1750 cm^{-1}), sp^2-hybridized C═C (in-plane stretching, ~1500−1600 cm^{-1}), and epoxides (C−O−C, ~1280−1330 and 800−900 cm^{-1}). The regions labeled as α (red), β (yellow), and γ (green) refer to the chemical species summarized in Table S5 (Supporting Information) for the overlapped infrared frequencies at 800−1500 cm^{-1}.

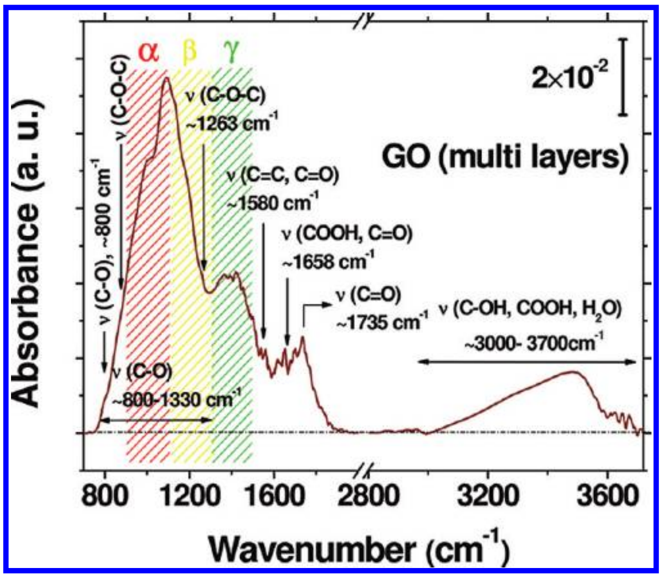

Figure 2. Transmission infrared absorbance spectrum of GO (multilayers) at room temperature. Vibrational modes are shown for hydroxyls with contributions from COOH and H_2O (C−OH, 3000−3700 cm^{-1}), ketones and/or carboxyls within the overlapped frequency range (C═O, COOH, ~1700−1900 cm^{-1}), sp^2-hybridized C═C (in-plane stretching, ~1550−1650 cm^{-1}), and epoxides (C−O−C, ~1350 and ~800−900 cm^{-1}). The regions labeled as α (red), β (yellow), and γ (green) refer to the chemical species summarized in Table S5 (Supporting Information) for the overlapped infrared frequencies at 800−1500 cm^{-1}.

randomly distributed oxygen functional groups located both at the edges and on the basal plane, a proper characterization and identification of the existing functional groups prior to any annealing is important and was carried out using in situ transmission infrared spectroscopy. Assignment of the measured infrared absorption spectra provides direct information on the type of oxygen species formed upon the oxidation process. For instance, Figures 1 and 2 and Figures S1 and S2 (Supporting Information) summarize results obtained on GO samples of different thicknesses (single, Figure S1, Supporting Information; three, Figure S2, Supporting Information; five, Figure 1, and multiple layers, Figure 2), all synthesized using Hummer's method[89] within the same batch of GO. For comparison, Figure S3 (Supporting Information) shows the spectrum of multilayered GO similarly synthesized (i.e., modified Hummer's method).[90] Experimental spectra recorded at room temperature are reproducible, indicating that, on average, the oxygen functionalities are similar from sample to sample. The only difference among them is the relative strengths of specific absorbance features corresponding to specific oxygen functional groups, suggesting that there is a quantitative difference possibly resulting from their random distribution. In general, the IR absorbance features are related to the chemical functionalities on both the edges and the basal plane of GO and their concentration depends on the synthesis conditions. For instance, the modified Hummer's method leads to strong infrared absorbance associated with the C═O/COOH and C−OH regions of multilayered GO with a sharp peak at 3000−3700 cm^{-1} due to larger hydroxyl, carboxyl, and water contribution (Figure S3 vs Figure S2, Supporting Information). Simply due to the number of layers (i.e., GO coverage on the substrate), the infrared absorbance is stronger for multilayered GO films (Figure 2 and Figure S3, Supporting Information) than for five, three, and single layers of GO (Figure 1 and Figures S1 and S2, Supporting Information). In all these figures, we use symbols "C−O, C−O−C, C═C, COOH, C═O, and C−OH" to generalize the derivatives of "ethers, epoxides, sp^2 carbon, carboxyls, ketones, and hydroxyls", respectively.

The random distribution of oxygen groups complicates the analysis of the infrared spectra because there is a range of environments for each species, leading to frequency shifts that are particularly difficult to deal with in the frequency regions where the modes overlap. We elucidate this by determining the effects of interactions in the stretching modes (Tables 1−4) using first-principles DFT calculations. Individual cluster models of specific oxygen species given in Tables S1−S4 (Supporting Information) are selected based on discussions in sections 2.1 and 2.2 and then simulated to determine conjugation, inductance, and resonance effects of aromatic and heterocyclic systems on infrared frequencies.[95] Infrared absorbance intensities for each individual cluster provide a semiquantitative measure of each functional group concentration for every specific assigned frequency. In Tables S1−S4 (Supporting Information), the modes are organized in the order of increasing intensities (1, the strongest, and 4, the weakest). Each simulated vibrational frequency is shown with its corrected values within ~50 cm^{-1} deviation from simulated frequencies (further information given in section 3.4).

A broad band for C−OH, apparent in the spectra of single (Figure S1, Supporting Information), three (Figure S2, Supporting Information), and five layers (Figure 1) of GO sharpens in the case of GO (multilayers) (Figure 2 and Figure S3, Supporting Information). It arises from the presence of hydroxyl (3000−3700 cm^{-1}) and carboxyl (~3550 cm^{-1}) groups as well as water. Indeed, there is a contribution from H_2O scissor modes at

Table 1. Summary of the Simulated and Experimental Vibrational Infrared Frequencies from Table S1 (Supporting Information)[a]

chemical species	simulated frequencies (cm^{-1})[c]	corrected frequencies (cm^{-1})
hydroxyls (basal plane phenol)	1125^{2}, 3670^{1}	1075, 3620
hydroxyls (edge phenol)	1090^{3}, 1145^{2}, 1166^{4}, 3745^{1}	1040, 1095, 1116, 3695
carboxyls	781^{1}, 1131^{4}, 1787^{3}, 3599^{2}	731[b], 1081, 1737, 3549
epoxides	767^{4}, 770^{2}, 896^{1}, 1120^{6}, 1220^{5}, 1370^{3}	717[b], 720[b], 846, 1070, 1170, 1320

[a] Corrected frequencies are expected experimental values derived from simulated frequencies (subtraction of ∼50 cm^{-1}). The frequencies are ordered with respect to the simulated IR intensities. [b] IR frequencies are not used due to interference from Si phonon modes. [c] Numbers correspond to the orders in terms of the simulated IR intensities (i.e., the strongest is “1”, the weakest is “4”).

Table 2. Summary of the Simulated and Experimental Vibrational Infrared Frequencies from Table S2 (Supporting Information)[a]

chemical species	simulated frequencies (cm^{-1})[c]	corrected frequencies (cm^{-1})
ketones	864^{4}, 1290^{3}, 1503^{1}, 1536^{2}	814, 1240, 1453, 1486
1,2-benzoquinones	852^{2}, 1273^{4}, 1705^{1}, 1734^{3}	802, 1223, 1655, 1684
1,3-benzoquinones	845^{2}, 1526^{1}, 1573^{3}	795[b], 1476, 1523
benzo[*de*]chromene-2,3-diones	763^{1}, 1209^{3}, 1699^{2}	713[b], 1159, 1649
acid anhydrides	676^{1}, 1046^{4}, 1182^{2}, 1767^{3}, 1802^{5}	626[b], 996, 1132, 1717, 1752

[a] Corrected frequencies are expected experimental values derived from simulated frequencies (subtraction of ∼50 cm^{-1}). The frequencies are ordered with respect to the simulated IR intensities. [b] IR frequencies are not used due to interference from Si phonon modes. [c] Numbers correspond to the orders in terms of the simulated IR intensities (i.e., the strongest is “1”, the weakest is “4”).

Table 3. Summary of the Simulated and Experimental Vibrational Infrared Frequencies from Table S3 (Supporting Information)[a]

chemical species	simulated frequencies (cm^{-1})[c]	corrected frequencies (cm^{-1})
2-pyranones (pyrone)	661^{2}, 1709^{1}	611[b], 1659
naptho[1,8-*de*][1,3]dioxin-2-ones	724^{1}, 1123^{2}, 1863^{3}	674[b], 1073, 1813
γ-butyrolactones	699^{2}, 721^{1}, 1247^{3}, 1854^{4}	649[b], 671[b], 1197, 1804
five-membered-ring lactols	779^{4}, 999^{2}, 1181^{3}, 3669^{1}	729[b], 949, 1131, 3619

[a] Corrected frequencies are expected experimental values derived from simulated frequencies (subtraction of ∼50 cm^{-1}). The frequencies are ordered with respect to the simulated IR intensities. [b] IR frequencies are not used due to interference from Si phonon modes. [c] Numbers correspond to the orders in terms of the simulated IR intensities (i.e., the strongest is “1”, the weakest is “4”).

Table 4. Summary of the Simulated and Experimental Vibrational Infrared Frequencies from Table S4 (Supporting Information)[a]

chemical species	simulated frequencies (cm^{-1})[c]	corrected frequencies (cm^{-1})
dioxolanes	1086^{1}, 1114^{2}	1036, 1064
peroxides	618^{1}, 978^{2}, 1235^{4}, 1317^{3}	568[b], 928, 1185, 1267
ethers (pyran-like)	557^{1}, 719^{3}, 1153^{4}, 1372^{2}	507[b], 669[b], 1103, 1322
ethers (furan-like)	680^{2}, 1053^{1}, 1115^{3}, 1329^{3}	610, 1003, 1065, 1279

[a] Corrected frequencies are expected experimental values derived from simulated frequencies (subtraction of ∼50 cm^{-1}). The frequencies are ordered with respect to the simulated IR intensities. [b] IR frequencies are not used due to interference from Si phonon modes. [c] Numbers correspond to the orders in terms of the simulated IR intensities (i.e., the strongest is “1”, the weakest is “4”).

1600−1750 cm^{-1}, unambiguously confirming that water molecules are either intercalated among the stacks of GO or physisorbed on the surface of GO sheets. In this broad band above 3000 cm^{-1}, there are contributions involving the C−OH stretch at 3549, 3619, 3620, and 3695 cm^{-1}, which are attributed to carboxyls, five-membered-ring lactols, and hydroxyls (on both the basal plane and the edge hydroxyls), respectively, with an additional C−OH stretch of trapped water. Epoxides (1280−1320 cm^{-1}) are also present with a specific contribution at ∼850 cm^{-1}, which is consistent with the simulated IR frequency (896 cm^{-1}, Table S1d, Supporting Information). Although the simulated frequency for this mode is at 1320 cm^{-1}, the epoxide peak is initially observed at 1280 cm^{-1} and falls within the frequency range of ∼1280−1320 cm^{-1}. Because the IR cross section of the C−OH mode of the carboxyl groups (COOH) is stronger than the C=O stretch of ketones, their contribution dominates. There is also a band at 1500−1600 cm^{-1} that is not related to oxygen groups, namely, the asymmetric stretch of sp^{2}-hybridized C=C. Its intensity critically depends on the environment, being strongest when out-of-plane species are removed, restoring the C=C bonds, but edge termination remains (e.g., carboxyls, carbonyls). This mode overlaps with C=O vibrations of ketones and 1,3-benzoquinones (Table 2) as well. The stretching vibrational modes of all the other derivatives of ketone groups (Tables 2 and 3) fall in higher-frequency regions (1750−1850 cm^{-1}) with contributions at 800−1600 cm^{-1} overlapped within ether (800−1322 cm^{-1}, Table 4) and C=C (1500−1600 cm^{-1}) regions.

Many of the above chemical species have more than one contribution (weaker in intensities) in the regions labeled α (900−1100 cm^{-1}), β (1100−1280 cm^{-1}), and γ (1280−1500 cm^{-1}); that is, there is overlap of modes from several distinct species within each region, as summarized in Table S5 (Supporting Information). Table S5 indicates that the ethers (peroxides, furans, dioxolanes) dominate at the α region with weaker contributions from hydroxyls and carboxyls, whereas weak absorptions of ketones (mainly pyrones and γ-butyrolactones) are more likely to fall in the β region, although peroxides (1267, 1185 cm^{-1}) and pyrans (1103 cm^{-1}) also contribute to the β region. Both of these groups have modes in the γ region, where the epoxides are the most common groups, following with ketones and 1,3-benzoquinones (1453−1523 cm^{-1}). Although epoxides fall in the γ region (~1320 cm^{-1}), some of their additional weak vibrational modes are present in α (1070 cm^{-1}) and β (1170 cm^{-1}) regions as well. Five-membered-ring lactols can only be identified from α and β regions with modes at ~949 and 1131 cm^{-1}, including an additional contribution at ~3620 cm^{-1} (Table 3) in the hydroxyl stretch region. Dioxolanes can only be characterized from α regions with two peaks at 1036 and 1064 cm^{-1}. Additional weak vibrational modes of both carboxyls (1081 cm^{-1}) and hydroxyls (1040−1095 cm^{-1}) are only present in the α regions. Apart from the weak peak contributions, the strongest infrared band of carboxyls is located at ~1600−1750 cm^{-1}, as part of a broad band with contributions from C=C (1500−1600 cm^{-1}) and C=O (1750−1850 cm^{-1}). It is also likely to have the stretching mode contributions of C=O in the COOH region due to 1,2-benzoquinones (1655−1684 cm^{-1}), benzo[*de*]chromene-2,3-diones (1649 cm^{-1}), acid anhydrides (1717 cm^{-1}) summarized in Table 2, and pyrones (1659 cm^{-1}, Table 3).

The shapes and widths of the bands give information about the concentration of each oxygen species specific to each sample under consideration. For instance, infrared absorbance is the strongest in the α region of GO-5 L (Figure 1) and in multilayered GO (Figure 2 and Figure S3, Supporting Information), indicating that the contribution from C−O (all ether derivatives) and C−OH (all hydroxyls and species with OH groups) dominates with a relatively smaller contribution from COOH (carboxyls) and C=O (all ketone derivatives). In contrast, samples prepared from the same batch of GO solution, but deposited into a single layer only (Figure S1, Supporting Information, GO-1 L), present a much stronger COOH contribution, with relatively weaker C−OH and C=O contributions. Indeed, GO-3 L does have strong infrared absorbance intensity for COOH as in the same level of infrared absorbance in α and β regions. The strongest absorbance for all samples (single layer to multilayers) in frequency regions with a large overlap (900−1500 cm^{-1}) is observed in both α and β regions (the contribution from epoxides is the strongest in β regions of both GO-1 L and GO-3 L samples and less intense in the GO-5 L and GO-ML samples). The presence of water molecules trapped in the interlayers or physisorbed on the film surfaces broadens the band associated with C−OH at ~3000−3700 cm^{-1}. Their effect on the hydrogen-bond network of other existing oxygen functionalities also modifies the infrared absorbance intensity and may be responsible for the increased intensity of the O−H stretch of C−OH in GO-ML (Figure S3, Supporting Information). This experimental observation indicates that there is a large concentration of hydroxyls in this specific sample in comparison with GO-ML in Figure 2.

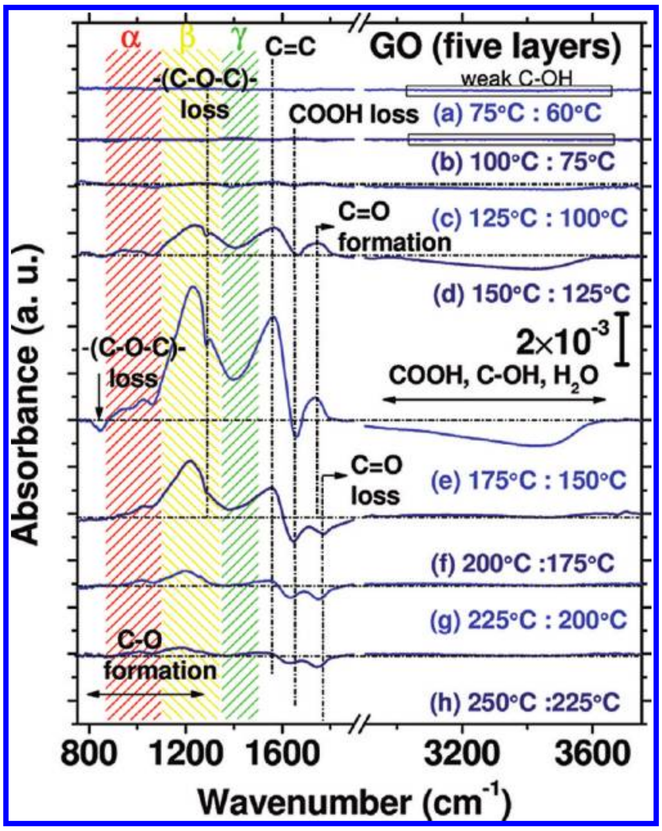

Figure 3. Transmission infrared differential spectra of GO (five layers) in the low-temperature regime (60−250 °C). Changes of functional groups are shown at the following temperatures: (a) 60−75, (b) 75−100, (c) 100−125, (d) 125−150, (e) 150−175, (f) 175−200, (g) 200−225, and (h) 225−250 °C. −(C−O−C)−, COOH, C=O, C−O, C−OH, and C=C represent epoxides, carboxyls, ketones, ethers, hydroxyls, and sp^2-hybridized C=C, respectively. The negative peaks below the baseline (black dotted lines) show the disappearance (loss) and the positive ones above it represent new formation of the functional groups with respect to each annealing temperature. The regions labeled as α, β, and γ present the overlapped frequencies of many functional groups (Table S5, Supporting Information) with red, yellow, and green patterned lines, respectively.

So far, we have analyzed each individual spectrum of GO samples and compared the initial concentration of oxygen species using cluster-model simulated frequencies without taking into account the conjugation effect of the sp^2-hybridized C=C backbone on the vibrational frequencies, which may lead to shifts of 30−40 cm^{-1} due to oxygen interactions. Therefore, further assignments, checks for corrections in these assignments especially for the overlapped regions, are required. These qualitative experimental findings will be further combined with a quantitative analysis using fittings for each individual oxygen peak to bring a detailed understanding of the thermal annealing process in the following sections.

4.2. Structural Evolution of GO during Thermal Annealing. We examine the evolution of oxygen species during thermal annealing by analyzing the IR absorption spectra using DFT-based simulations. The data are best represented by differential spectra, obtained by subtracting the spectrum at the last annealing temperature to that obtained at the new temperature. Thus, a negative absorption corresponds to a loss or decomposition of functional groups and a positive absorption indicates the formation of intermediate functional groups. For consistency, all annealing cycles were performed for exactly 5 min at each temperature. Longer annealing times lead to larger removal or changes of oxygen groups, which will be discussed later. In addition to the spectral analysis based on DFT simulations, we extract semiquantitative information of the amount of remaining oxygen groups using infrared absorbance peaks. For this purpose, infrared differential spectra corresponding to anneals from 60 to 850 °C were collected for single,[30] three,[26] five (Figures 3 and 5), and multiple layers (Figures 4 and 6) of GO samples. We present the data in three different temperature regions, low- (60−250 °C), moderate- (250−650 °C), and high- (650−850 °C) temperature regimes, and summarize the results in Table 5.

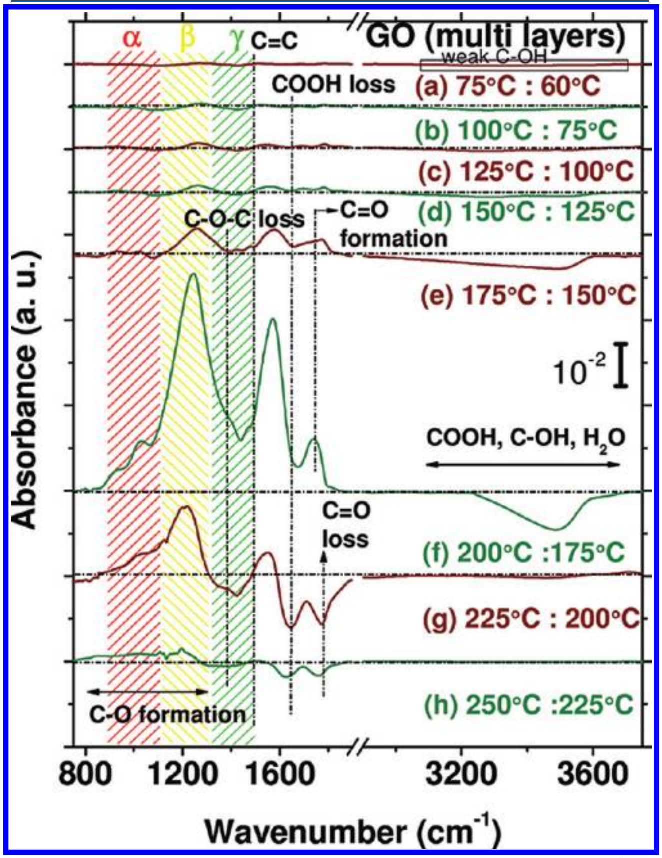

Figure 4. Transmission infrared differential spectra of GO (multilayers) in the low-temperature regime (60−250 °C). Changes of functional groups are shown at the following temperatures: (a) 60−75, (b) 75−100, (c) 100−125, (d) 125−150, (e) 150−175, (f) 175−200, (g) 200−225, and (h) 225−250 °C. −(C−O−C)−, COOH, C═O, C−O, C−OH, and C═C represent epoxides, carboxyls, ketones, ethers, hydroxyls, and sp^2-hybridized C═C, respectively. The negative peaks below the baseline (black dotted lines) show the disappearance (loss) and the positive ones above it represent new formation of the functional groups with respect to each annealing temperature. The regions labeled as α, β, and γ present the overlapped frequencies of many functional groups (Table S5, Supporting Information) with red, yellow, and green patterned lines, respectively.

4.2.1. Low-Temperature (60−250 °C) Spectra and Assignments. Infrared differential spectra of GO (five layers and multilayers) (Figures 3−6) show spectral changes during thermal annealing at temperatures of 60−250 °C. A decomposition of the oxygen groups is observed at lower temperatures (i.e., no formation of intermediate oxygen species), except for GO-ML. In GO-5 L, the decomposition of hydroxyls is initiated at 100 °C, followed by the removal of epoxides (125 °C), carboxyls (150 °C), and ketones (175 °C) (Figure 3, spectra a−f). The loss of epoxides at ∼1280−1320 cm^{-1} (with a weaker additional loss at ∼846 cm^{-1}) and hydroxyls at ∼3100−3700 cm^{-1} could not be observed at temperatures higher than 200 °C (Figure 3, spectrum f). On the other hand, removal of the carboxyls and ketones continues even at 250 °C (Figure 3, spectra g−h). The loss of hydroxyls starts at low temperatures (75 °C) with a small change up to 150 °C, followed by the decomposition of epoxides (175 °C), carboxyls (175 °C), and ketones (225 °C) of layers of GO (Figure 4, spectra a−f). These experimental observations suggest that the epoxides, carboxyls, and ketones decompose at higher temperatures than hydroxyls do. The removal of these groups also starts at higher temperatures in multilayered GO in comparison with five-layered GO (Table 5). This is associated with the strong oxygen interactions due to the participation of other nearby chemical species. Further, the oxygen groups of GO-ML dissociate continuously until 250 °C (Figure 4, spectra g−h) with the exception of epoxides that disappear at 225 °C. In the meantime, new intermediate species, such as ketones and ethers, start forming at 125 °C, shown with weak and broad absorptions at ∼800−1850 cm^{-1}, and at 150 °C (Figure 3, spectra d and e) in GO-5 L, respectively. The formation of these oxygen groups are also observed in GO-ML (Figure 4, spectrum b)

Table 5. Summary of the Thermal Reduction Process

temperature range (°C)	GO (single layer)	GO (three layers)	GO (five layers)	GO (multilayers)
low *T* (60−250 °C)	epoxide loss (100−200 °C)	epoxide loss (125−175 °C)	epoxide loss (125−200 °C)	epoxide loss (150−225 °C)
	COOH loss (100−250 °C)	COOH loss (125−250 °C)	COOH loss (150−250 °C)	COOH loss (175−250 °C)
	C═O loss (200−250 °C)	C═O loss (150−250 °C)	C═O loss (175−250 °C)	C═O loss (200−250 °C)
	C−OH loss (100−150 °C)	C−OH loss (100−175 °C)	C−OH loss (100−200 °C)	C−OH loss (75−250 °C)
	C═O formation (125−175 °C)	C═O formation (100−175 °C)	C═O formation (125−175 °C)	C═O formation (75−175 °C)
	C−O formation (100−250 °C)	C−O formation (100−250 °C)	C−O formation (150−250 °C)	C−O formation (75−250 °C)
	COOH loss (275−400 °C)	COOH loss (250−400 °C)	COOH loss (250−600 °C)	COOH loss (250−650 °C)
moderate *T* (250−650 °C)	C═O loss (275−400 °C)	C═O loss (250−600 °C)	C═O loss(250−650 °C)	C═O loss (250−650 °C)
	C−OH loss (275−350 °C)	C−OH loss (300−350 °C)	C−OH loss[a] (250−350 °C)	C−OH loss[a] (250−350 °C)
	C−O loss (250−650 °C)	C−O loss (250−650 °C)	C−O loss (250−650 °C)	C−O loss (250−650 °C)
high *T* (650−750 °C)	remaining C−O	remaining C−O	remaining C−O and C═O	remaining C−O and C═O

[a] Minor hydroxyl desorption, broad peak, and weak infrared intensity in the diffential spectra.

Table 6. Summary of the Simulated and Experimental Vibrational Infrared Frequencies from Table S6 (Supporting Information)[a]

chemical species	simulated frequencies (cm^{-1})[b]	corrected frequencies (cm^{-1})
COOH + COOH	760^1, 1145^3, 1792^2, 3592^5, 3595^4	710, 1095, 1742, 3542, 3545
OH + COOH	760^4, 1114^5, 1781^3, 3611^2,3711^1	710, 1064, 1731, 3561, 3661
COOH + C=O	740^3, 1114^4, 1759^1, 3625^2	690, 1064, 1709, 3575
OH + C=O	1222^1, 1415^5, 1513^3, 1535^5, 1591^4, 1825^2	1172, 1365, 1463, 1485, 1541, 1775
C=O + C=O	650^5, 842^3, 1342^4, 1521^1, 1543^2	600, 792, 1292, 1471, 1493
OH + OH	1130^4, 1321^3, 1530^5, 3412^1, 3706^2	1080, 1271, 1480, 3362, 3646

[a] Corrected frequencies are expected experimental values derived from simulated frequencies (subtraction of ~50 cm^{-1}). The frequencies are ordered with respect to the simulated IR intensities. [b] Numbers correspond to the orders in terms of the simulated IR intensities (i.e., the strongest is "1", the weakest is "4").

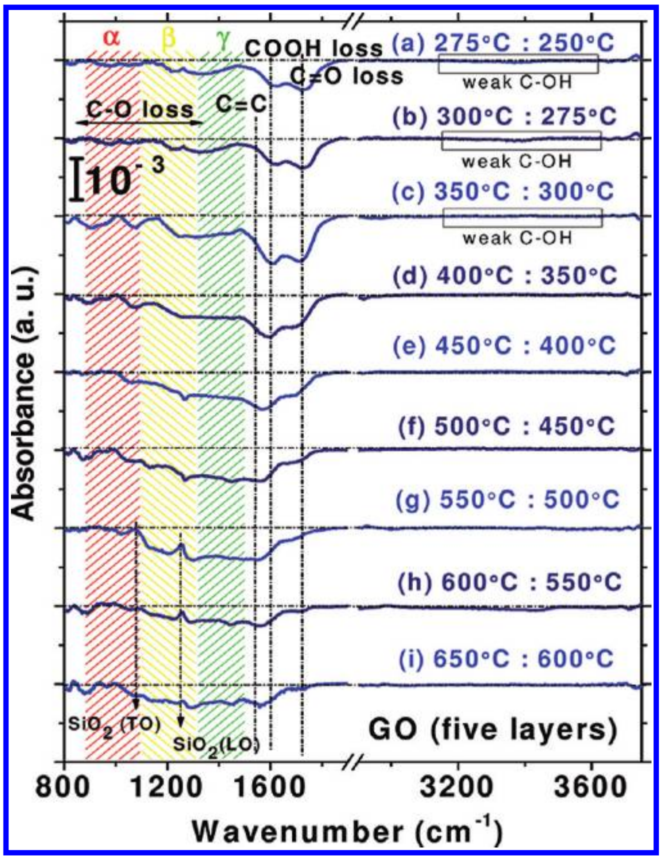

Figure 5. Transmission infrared differential spectra of GO (five layers) at moderate temperatures (250−650 °C). Changes of functional groups are shown at the following temperatures: (a) 250−275, (b) 275−300, (c) 300−350, (d) 350−400, (e) 400−450, (f) 450−500, (g) 500−550, (h) 550−600, and (i) 600−650 °C. −(C−O−C)−, COOH, C=O, C−O, and C=C represent epoxides, carboxyls, ketones, ethers, and sp^2-hybridized C=C, respectively. The negative peaks below the baseline (black dotted lines) show the disappearance (loss) and the positive ones above it represent new formation of the functional groups with respect to each annealing temperature. The regions labeled as α, β, and γ represent the overlapped frequencies of many functional groups (Table S5, Supporting Information) with red, yellow, and green patterned lines, respectively.

at temperatures as low as 75 °C. The formation of new ketone groups is observed and continues until 175 °C, while ethers form and increase until 200 °C. Overall, the IR absorbance in β and γ regions increases in multilayered GO, although there is clearly a

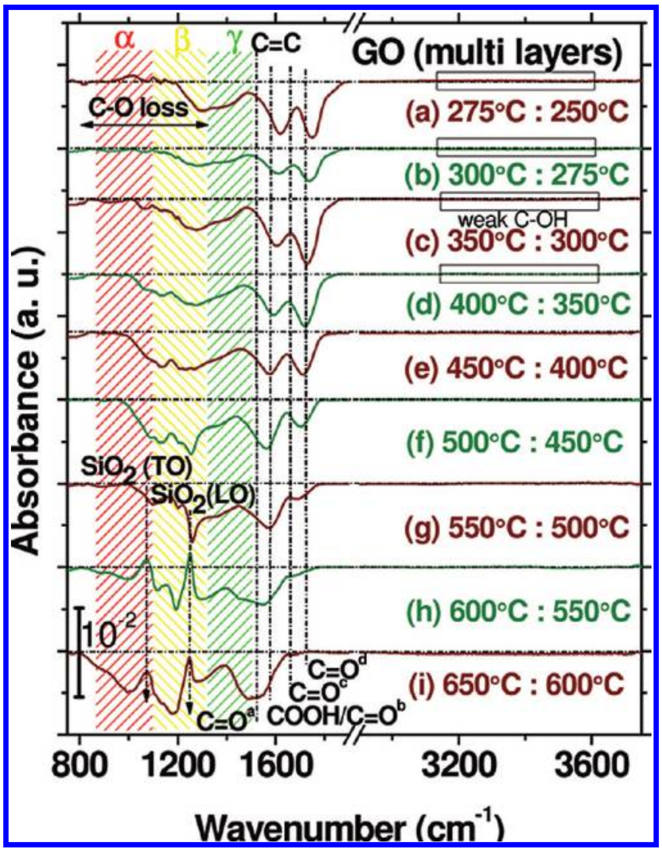

Figure 6. Transmission infrared differential spectra of GO (multilayers) at moderate temperatures (250−650 °C). Changes of functional groups are shown at the following temperatures: (a) 250−275, (b) 275−300, (c) 300−350, (d) 350−400, (e) 400−450, (f) 450−500, (g) 500−550, (h) 550−600, and (i) 600−650 °C. −(C−O−C)−, COOH, C=O, C−O, and C=C represent epoxides, carboxyls, ketones, ethers, and sp^2-hybridized C=C, respectively. The negative peaks below the baseline (black dotted lines) show the disappearance (loss) and the positive ones above it represent new formation of the functional groups with respect to each annealing temperature. The regions labeled as α, β, and γ present the overlapped frequencies of many functional groups (Table S5, Supporting Information) with red, yellow, and green patterned lines, respectively. Vibrational modes of SiO_2 (LO and TO modes) appear at ~1250 and 1080 cm^{-1}, respectively.

removal/evolution of other functional groups (e.g., epoxides). This is associated with the interactions of etch holes with trapped water molecules in the interlayers, leading to a strong infrared enhancement as a result of carbonyl formation.[26] In general, the experimental observations indicate that the removal of oxygen species is initiated earlier in single and three layers of GO samples due to weaker interlayer or edge interactions (Table 6), as previously described in refs 26 and 30. Furthermore, the epoxides and carboxyls start decomposing at 100 °C in a single layer of GO (see ref 30), as given in Table 5, earlier than all the other three (see ref 26), five, and multiple layers of GO, whereas carbonyls are removed at 200 °C. The main reason is the absence of trapped water in a single layer of GO, which is necessary for additional carbonyl formation.

4.2.2. Moderate-Temperature (250−650 °C) Spectra and Assignments. Infrared differential spectra of five- and multilayered GO are presented for moderate-temperature annealing (250−650 °C) in Figures 5 and 6, spectra a−i, respectively. As shown in these two spectra, the desorption of carboxyls, carbonyls, and ethers, initiated below 250 °C, continues to represent the main changes in the 250−650 °C annealing range. Decomposition of hydroxyls is minor for both reduced GO-5 L and GO-ML samples, as evidenced by a small loss of infrared absorbance after a 350 °C anneal, and it is all removed by 350 °C for both samples. Above 250 °C, there is a large loss of carboxyls and ketones observed in β and γ regions up to 650 °C for five- and multilayered GO. In contrast, the decomposition of carboxyls, ketones, and hydroxyls is completed at 400 °C for a single layer of GO (Table 5), except for ethers that remain in the structure at temperatures as high as 650 °C.[30] In three layers of GO (Table 5), the situation is intermediate, with ketones and carboxyls remaining above 400 °C and removed after a 650 °C anneal.[26] The only remaining oxygen group above 650 °C in GO-1 L and GO-3 L is in the ether configuration (Table 5). In contrast, Table 5 shows that ketone groups are still present in five- and multilayered GO even after a 650 °C anneal. It, therefore, seems that the concentration of oxygen groups throughout the annealing process depends on the initial starting amount of carboxyls and carbonyls (all ketone derivatives) at room temperature and the ability of hydroxyl radicals to attack on these groups, as discussed later.

The assignment of remaining contributions to the β and carbonyl spectral regions in five- and multilayered GO is accomplished using DFT simulations summarized in Tables 2 and 3. These simulations suggest that ethers exist in the form of either furans or pyrans. Indeed, the infrared frequencies shift to the lower-frequency region of carboxyls and carbonyls ($\sim$1600−1650 cm^{-1}), typical of ketones, diketones (1,2-benzoquinones, 1,3-benzoquinones, and benzo[*de*]chromene-2,3-diones), and pyrones. The carbonyl region is randomly divided into four frequency regions labeled as $C{=}O^a$ ($\sim$1400−1650 cm^{-1}), $C{=}O^b$ ($\sim$1650−1750 cm^{-1}), $C{=}O^c$ ($\sim$1750−1800 cm^{-1}), and $C{=}O^d$ ($\sim$1800−1850 cm^{-1}) to help distinguish ketone contributions in GO-ML (Figure 6) after annealing at 250−650 °C. The $C{=}O^a$ peak, which overlaps with the sp^2-hybridized C=C in-plane stretching mode ($\sim$1580 cm^{-1}), corresponds to the ketones, 1,3-benzoquinones, and benzo[*de*]chromene-2,3-diones. The $C{=}O^b$ peak involves contributions from 1,2-benzoquinones, benzo[*de*]chromene-2,3-diones, acid anhydrides, and pyrones. The $C{=}O^c$ peak is composed of contributions from both acid anhydrides and γ-butyrolactones. In addition, the $C{=}O^d$ peak represents vibrational modes of γ-butyrolactones and naphto[1,8-*de*][1,3]dioxin-2-ones. On the basis of these assignments, the only carbonyl contributions that remain after annealing at 650 °C are from $C{=}O^a$ and $C{=}O^b$. These experimental observations and tentative assignments will be used to further examine the oxygen interactions in GO samples in section 5.

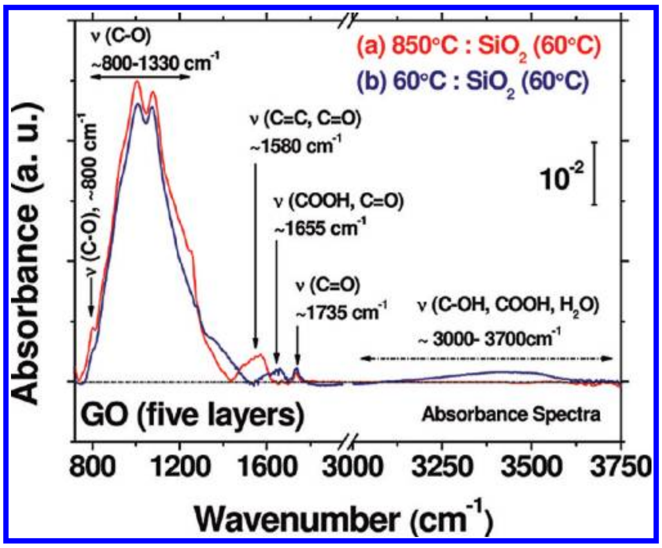

Figure 7. Transmission infrared absorbance spectra of GO (five layers). Changes in functional groups are given at temperatures of (a) 850 °C (red) and (b) 60 °C (blue) referenced to the initial clean SiO$_2$ surface.

4.2.2.1. Effects of Oxygen Species Arrangement on Spectral Properties. Our motivation for addressing the arrangement of oxygen species comes from Jeong et al.'s study showing a random distribution of functional groups.[96] The resulting "random" interactions tend to shift and broaden the infrared vibrational modes. Indeed, the vibrational frequencies of oxygen functional groups shift to either higher (blue shifts) or lower (red shifts) wavenumbers ($\sim$20−50 cm^{-1}) according to DFT simulations (Table 6 and Table S6, Supporting Information). This phenomenon is associated with the effect of London dispersion forces, hydrogen bonds, and dipole−dipole interactions among oxygen groups, such as carboxyls and hydroxyls, in addition to the effect of π-conjugation. For instance, when two COOH groups (Table S6a, Supporting Information) are next to each other, there is a blue shift of about $\sim$10 cm^{-1} from the original characteristic peak at $\sim$1742 cm^{-1} in comparison to the isolated COOH (Table 1). As a result, the two C−OH stretches of COOH bands appear at lower frequencies (3542, 3545 cm^{-1}). However, when one OH is located nearby a COOH (Table S6b, Supporting Information), this mode now appears at a lower frequency ($\sim$1731 cm^{-1}), that is, with having a $\sim$10 cm^{-1} red shift. In contrast, the C−OH modes (3561, 3661 cm^{-1}) are blue shifted.

A similar effect on infrared frequencies of COOH groups could be observed when there is a nearby C=O (Table S6c, Supporting Information). In particular, C=O groups are red shifted, taking them from the β region to the γ region. Hydroxyls also experience a small red shift, although their contribution remains in the α region. In all these cases, the C=O frequencies of the COOH groups do not go beyond 1750 cm^{-1}, which is consistent with other studies. For instance, Hadzi et al. assigned a band at 1720 cm^{-1} to nonconjugated carboxylic carbonyl groups,[97] and Szabó et al. showed that C=O stretching in carboxyl group could be observed at 1714 cm^{-1} using diffuse reflectance infrared Fourier transform (DRIFT) and deuterium-exchanged GO.[98] Moreover, carboxyl groups have additional weak contributions in only the α region (Table S7, Supporting Information), whereas hydroxyls weakly contribute to all the absorbance regions (α, β, and γ). Carbonyls, in contrast, contribute to the α region only if they are next to COOH groups. Furthermore, a contribution at higher frequency (~1775 cm^{-1}) can only be accounted for when there is one OH located nearby a C═O group (Table S6d, Supporting Information); for example, two neighboring C═O groups (Table S6e, Supporting Information) do not show such a high-frequency band. Another interaction effect is the peak broadening when one OH locates next to another OH, resulting from both through-bond interactions in addition to H-bonding in a range of ~3362−3656 cm^{-1} (Table S6f, Supporting Information). Despite all possible interactions and bonding configurations, the vibrational modes for C−OH or other O−H stretch are not observed at frequencies above ~3710 cm^{-1}.

4.2.3. High-Temperature (650−850 °C) Spectra and Assignments. Infrared differential spectra of five-layered GO annealed at 650−850 °C are given in Figure S4 (Supporting Information). Although there is some intensity loss in the β and γ regions and the C═O stretch mode after annealing at 750 °C (Figure S4, spectrum a, Supporting Information), there is a substantial contribution remaining for carbonyl species in the reduced five-layered GO (Figure 7, sample a). After annealing at 850 °C, most of these oxygen groups, such as hydroxyls, carboxyls (absence of C−OH peak), epoxides, carbonyls (except ketones and 1,3-benzoquinones), and some ethers, are removed (Figure S4, spectrum b, Supporting Information). As is evident in the absorbance spectra in Figure 7, there is no remaining absorption at ~1600−1750 cm^{-1} (COOH groups) and ~3000−3700 cm^{-1} (C−OH groups), confirming the removal or reaction of the carboxyl groups. The only remaining oxygen groups are in the form of ethers, ketones, and 1,3-benzoquinones, as shown by the absorbance spectra in Figure 7 (sample a). The weak contribution at ~1735 cm^{-1} is not due to COOH, but to C═O, because the conjugation effects are now mostly eliminated; that is, the C═O is expected at ~1735 cm^{-1}, whereas carboxyls would be expected at ~1700 cm^{-1}

Annealing to 850 °C has been shown to lead to dramatic changes in GO-1 L and GO-3 L, with the appearance of a sharp

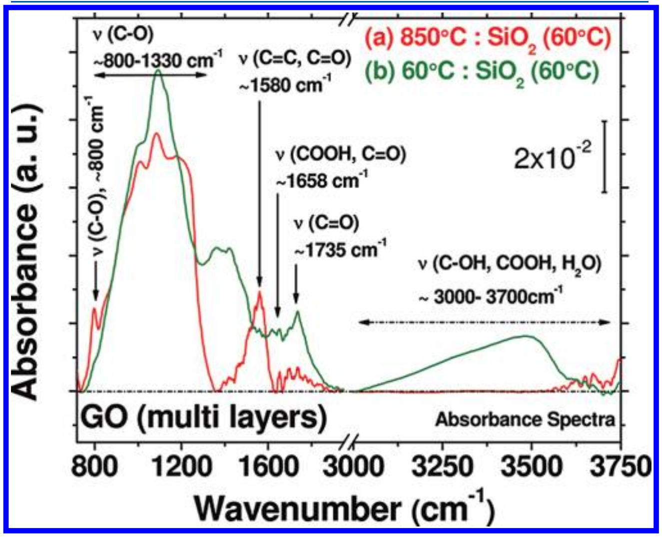

Figure 8. Transmission infrared absorbance spectra of GO (multilayers, thin). Changes of functional groups are given at temperatures of (a) 850 °C (red) and (b) 60 °C (green) referenced to the initial clean SiO_2 surface.

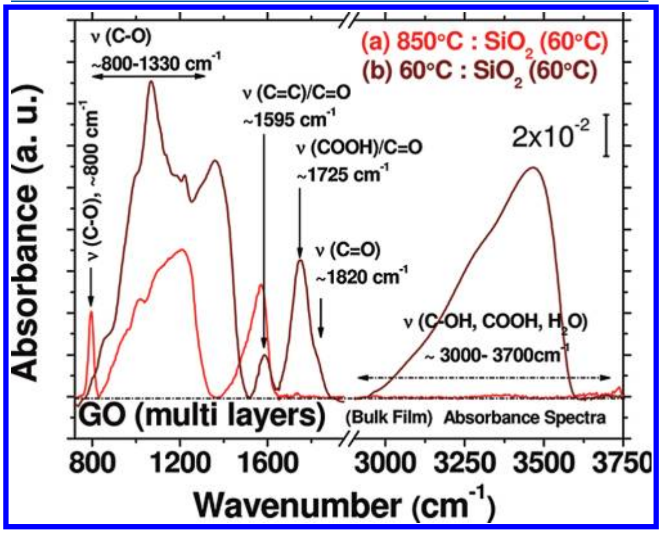

Figure 9. Tranmission infrared absorbance spectra of GO (multilayers, bulk). Changes of functional groups are given at temperatures of (a) 850 °C (red) and (b) 60 °C (brown) referenced to the initial clean SiO_2 surface.

Table 7. Summary of Integrated Infrared Absorbance (cm^{-1}) at Room Temperature for the Amount of Carbonyl (C═O, ~900−1850 cm^{-1}), Hydroxyl (C−OH, ~3000−3700 cm^{-1}), and Total Amount (800−3700 cm^{-1}) of Initial Starting Oxygen for Single, Three, Five, and Multiple Layers of GO and Their Corresponding fwhm Values (cm^{-1}) for the Peak at 800 cm^{-1} after an 850 °C Anneal

integrated absorbance (cm^{-1}) for oxygen species	GO-1 L	GO-3 L	GO-5 L (b)	GO-ML (thin)	GO-ML (bulk)
C═O + C−O	0.95	1.25	15.3[a]	42.7[a]	68.3[a]
C−OH (H_2O)	0.22	0.27	0.58	5.56	34.8
total oxygen	1.30	1.60	17.4	48.3	103.1
C═O/total (%)	73 ± 0.05	78 ± 0.03	88 ± 0.02	88 ± 0.01	66 ± 0.05
C−OH/total (%)	17 ± 0.02	17 ± 0.01	3 ± 0.03	12 ± 0.01	34 ± 0.03
remaining O (at. %)[b]	3−5	5−8	92	55	46
fwhm (cm^{-1})	80	100	50	44	32

[a] Integrations were performed at 800−1850 cm^{-1} due to overlapped peak at 800 cm^{-1} attributed to the C−O contribution. [b] Remaining oxygen is reported for annealing at 850 °C.

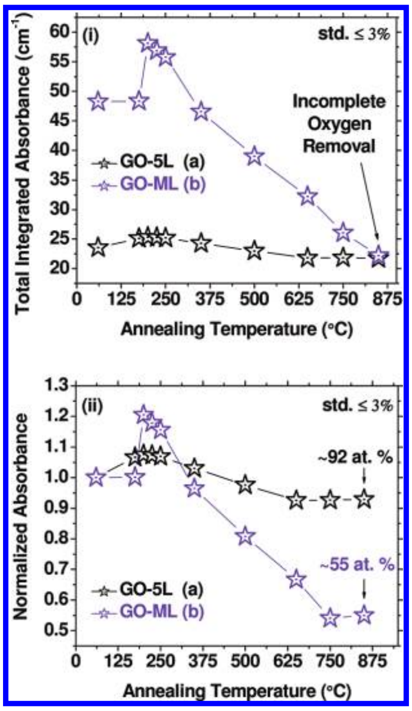

Figure 10. Integrated infrared absorbance of five- (a) and multilayered (b) GO synthesized using Hummers' method. (a) GO-5 L is shown for sample b. (b) GO-ML represents the thin multilayered GO. Comparison of the (i) total integrated absorbance and (ii) normalized absorbance with the initial amount of oxygen (~23.4 cm^{-1} for GO-5 L and ~48.3 cm^{-1} for GO-ML) is shown.

and enhanced absorption at 800 cm^{-1}.[30,26] This mode has been attributed to edge ether termination when all other oxygen functionalities are removed. The enhancement critically depends on the removal of these other functionalities and the degree of alignment of the edges. For GO-5 L (Figure S4, spectrum b, Supporting Information) and GO-ML (Figure S5, spectrum b, Supporting Information), the situation is different. In particular, there are now substantial contributions in the (1) α region, associated with the remaining ethers in the form of peroxides, furans, and dioxolanes, and (2) in the β and γ regions from pyrans, ketones, and 1,3-benzoquinones since hydroxyls and carboxyls are all removed.

The remaining oxygen species in the form of both ethers and carbonyls after annealing at 850 °C greatly reduce the intensity because not all other oxygen functionalities are removed (Figures 7, sample a, and 8, sample a). The full width at half-maximum (fwhm) is observed to decrease (50, 44, and to 32 cm^{-1}) for GO-5 L, GO-ML, (thin) and GO-ML (bulk), as shown in Figures S4−S6 (Supporting Information), respectively, as the amount of remaining oxygen functionalities in the form of both $C-O$ and $C=O$ in the reduced GO films decreases (Table 7). Both differential (Figures S7 and S8, Supporting Information) and absorbance spectra (Figures 7−9) show that the ethers and carbonyls still remain in multilayered GO after annealing at 850 °C. The infrared absorbance weakens in the γ region, shown with the absorbance spectrum in Figure 8, sample a. This remaining contribution is due to ethers since hydroxyls near either carbonyls or other OH groups are removed (Table S7, Supporting Information). Similarly, a comparison of the overall absorbance in Figure S6 (Supporting Information) and Figure 9 indicates that more oxygen is removed in the thicker multilayered GO (a bulk film) compared to the thin film of multilayered GO in Figure 8, because less oxygen was initially present in the thicker sample (Figure 9).

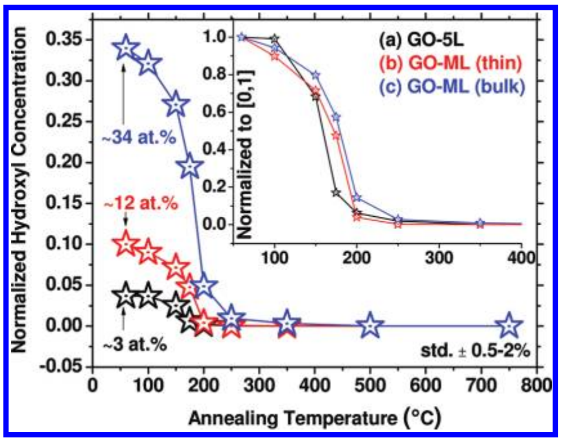

Figure 11. Hydroxyl concentration normalized to the initial amount of oxygen at room temperature versus annealing temperature. Each data point of GO-5 L (sample b), GO-ML (thin), and GO-ML (bulk) is normalized to 17.4, 48.3, and 103.1 cm^{-1}, respectively. The inset shows the following normalized data points to [0,1] for comparison.

5. DISCUSSION ON THE STRUCTURAL EVOLUTION OF GO

A quantitative analysis using both infrared absorbance and differential spectra is needed to determine the amount of oxygen species and to understand the spectral changes observed during thermal annealing from room to high temperatures in GO samples with different starting thicknesses. There are also questions to be answered, such as "how much oxygen remains after annealing" and "how the leftover oxygen affects the spectral interpretations", together with the concerns about "why the enhancement of the 800 cm^{-1} IR absorption band is less than expected". We will address all these questions in a more quantitative fashion by fitting the infrared peaks for each oxygen species to correlate the amount of existing oxygen to the integrated areas of the peaks. This analysis will be further discussed in the next three sections to clarify the issues related to the incomplete oxygen removal even with anneals at high temperatures, such as 850 °C, due to the influence of (1) the initial amount of total hydroxyl groups, (2) effects such as "densing" at the sheet edges with initial blocking with carboxyls and carbonyls and further oxygen removal and reactions at the etch holes, leading to additional carbonyl formation, (3) defect formation, and (4) of the time of thermal reduction.

5.1. Effect of Total Initial Oxygen Concentration. The thermal reduction of both five- and multilayered GO thin films remains incomplete, with ~92 and 55 at. % of oxygen leftover of the initial starting amount after annealing at 850 °C for 5 min, as shown in Figure 10 and in Table 7. In contrast, there is only 3−8 at. % of the initial oxygen that remains in the single and three layers of GO.[26,30] To understand the origin of this incomplete oxygen removal, it is important to examine the effect of several factors, such as (1) the initial amount of total oxygen in the samples, (2) the influence of the sample thickness, (3) the initial percentages of carboxyls, carbonyls, and hydroxyls out of the total initial amount of oxygen and

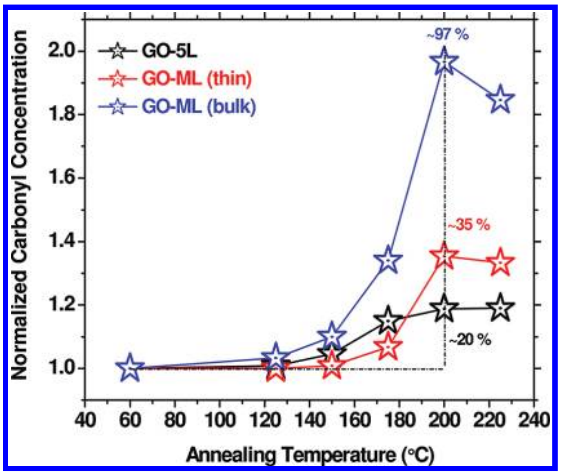

Figure 12. Carbonyl concentration normalized to the initial amount of oxygen at room temperature versus annealing temperature. Each data point of GO-5 L (sample b), GO-ML (thin film), and GO-ML (bulk film) is normalized to 15.3, 42.7, and 68.3 cm^{-1}, respectively.

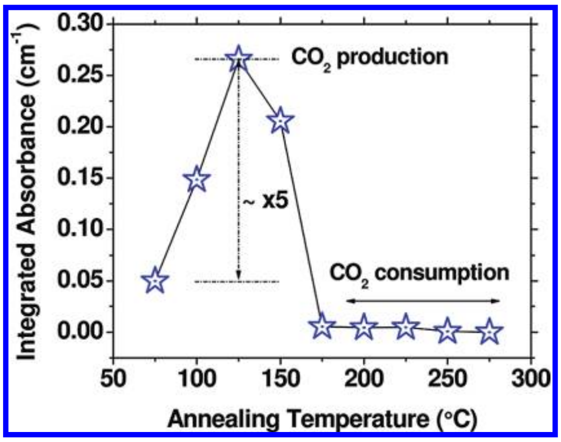

Figure 13. Integrated absorbance versus annealing temperature for multilayered GO. Integrated infrared absorbance showing CO_2 production during annealing (60−275 °C).

trapped water molecules at room temperature, and (4) reactions of water molecules and radicals with etch holes, generating an additional amount of carbonyls at intermediate temperatures.

5.1.1. Initial Oxygen Amount. Although the initial amount of oxygen at room temperature varies from sample to sample of nominally the same average thickness, the analysis of the data shows that this is not a dominant factor; that is, it does not directly determine the resulting amount of remaining oxygen upon thermal reduction. For instance, we examine two different GO-5 L samples (samples a and b as shown in Figure S7, Supporting Information) by calculating the total integrated absorbance to determine the initial absolute amounts of oxygen and the remaining amount of oxygen after annealing at 850 °C for 5 min. Although the initial amount of total oxygen at room temperature is slightly different in these samples (~23.4 cm^{-1} for sample a and ~17.4 cm^{-1} for sample b), the normalized absorbance with the initial amount of oxygen is similar, corresponding to the remaining oxygen percentages (~93 and ~92 at. %, respectively) after annealing at 850 °C.

5.1.2. Sample Thickness. The effects of the average sample thickness (number of layers) can also be ruled out by examining two different samples of multilayered GO, as shown in Figure S8 (Supporting Information). The total absorbance of integrated areas for the bulk GO-ML is ~103.6 and ~48.3 cm^{-1} for the thin GO-ML. Although the initial total amount of oxygen at room temperature is much larger in the bulk film of GO-ML (Figure S8, sample a, Supporting Information), the resulting amount of oxygen after annealing at 850 °C is much less (~46 at. %) compared to that of the thin film of GO-ML (Figure S8, sample b, Supporting Information, ~55 at. %). Therefore, the film thickness is not a major factor in determining the resulting amount of oxygen.

5.1.3. Effect of Carbonyls and Hydroxyls. The relative amounts of hydroxyls, carboxyls, and carbonyls per initial total oxygen play an important role at intermediate annealing temperatures. The resulting amount of oxygen and the efficiency of oxygen removal during the thermal reduction process appear to depend directly on their initial relative concentrations. Table 7 summarizes the initial amount of oxygen (atomic %) extracted from the integrated absorbance (cm^{-1}) for hydroxyls and carbonyls. The total initial hydroxyl concentration in GO-ML (~0.12 cm^{-1}, ~12 at. %) is much larger than that in GO-5 L (~0.03 cm^{-1}, 3 at. %). The total initial amount of water is also seen to scale with the initial hydroxyl amount and is substantially more for GO-ML. Therefore, even when the initial carbonyl concentrations are the same (~88 at. %) in both of these samples, the amount of initial total hydroxyl concentration changes the thermal reduction efficiency completely. After annealing at 850 °C, there is much more oxygen remaining (incomplete oxygen removal with ~92 at. % of initial total oxygen) in GO-5 L compared with thin GO-ML (~55 at. %) sample. This is because ~3 at. % of hydroxyl concentration in the GO-5 L sample is not enough for the edges for further propagation (Figure 11). Consequently, there is much less oxygen remaining in the reduced thin GO-ML (~55 at. %) sample than in GO-5 L (~92 at. %), although there was nearly 3 times more oxygen initially in the thin GO-ML (48.3 cm^{-1}) sample than in GO-5 L (17.4 cm^{-1}). This dependence on carbonyl and hydroxyl concentrations is also observed in bulk GO-ML that is much thicker than the thin GO-ML described above. For this bulk GO-ML sample, the edges are functionalized with much less carbonyls (~66 at. %) compared to the thin GO-ML (~88 at. %) sample, although there is nearly 3 times more hydroxyl concentration in total in the bulk GO-ML (~34 at. %) sample. The larger amount of hydroxyls, which increases the efficiency of C═O elimination, combined with the lower carbonyl concentration in the bulk GO-ML leads to lower amounts of oxygen remaining in the reduced bulk GO-ML (~46 at. %) than in the thin GO-ML (~55 at. %) after annealing at 850 °C for 5 min.

In contrast, the GO-1 L and GO-3 L samples have a much higher total initial hydroxyl concentration (~17 at. % C−OH of the initial total oxygen) compared with both the GO-5 L (3 at. %) and the thin GO-ML (12 at. %) samples. Because the amount of initial carbonyl concentration is larger in GO-3 L (~78 at. % of the initial total oxygen) than GO-1 L (~73 at. % of the initial total oxygen) and the initial total hydroxyl concentration is the same (~17 at. %), the remaining amount of oxygen in the reduced GO-3 L sample is larger (5−8 at. %) than that in GO-1 L (3−5 at. %). This process is mediated by the amount of trapped water relative to the initial total amount of oxygen, which is necessary for the propagation reactions described in Figure 16ii(b), both at

Table 8. Summary of the Simulated and Experimental Vibrational Infrared Frequencies from Table S8 (Supporting Information)[a]

chemical species	simulated frequencies (cm^{-1})[b]	corrected frequencies (cm^{-1})
1C vacancy	854^2, 1024^4, 1172^1, 1209^2, 1346^3	804, 974, 1122, 1159, 1296
2C vacancy	1117^1, 1154^3, 1287^2	1067, 1104, 1237

[a] Corrected frequencies are expected experimental values derived from simulated frequencies (subtraction of ~50 cm^{-1}). The frequencies are ordered with respect to the simulated IR intensities. [b] Numbers correspond to the orders in terms of the simulated IR intensities (i.e., the strongest is "1", the weakest is "4").

the etch holes and at the sheet edges, leading to C═O formation during thermal annealing. These propagation reactions involve carbonyl formation at intermediate temperatures. It is, therefore, important to identify how much additional carbonyl is formed at intermediate temperatures compared to the high temperature regimes, as discussed in the next section.

5.2. Effect of Additional Carbonyl Formation at Etch Holes. There are two dominant factors that determine the degree of intermediate-step carbonyl formation at the etch holes: (1) The ratio of the initial total hydroxyl concentration to the total initial amount of oxygen, which provides information for the initial amount of trapped water in the interlayers, as previously discussed. (2) The percentage of trapped water correlated with the additional amount of total carbonyls that are formed after annealing at moderate temperatures (100−250 °C) in addition to the initial carbonyl concentration at room temperature. In one of our recent studies,[26] we have shown that carbonyls are likely to form as a result of chemical reactions between the trapped water in the interlayers and the etch holes. Initially, the carbonyl concentration in both COOH and C═O forms is higher (~88 at. %) in both the GO-5 L and the thin GO-ML samples than in bulk GO-ML (~66 at. %), as shown in Table 7. Because carbonyls are reasonably stable oxygen configurations (with binding energies of 5.8 eV/COOH, 8.0 eV/C═O, respectively),[30] they remain at intermediate annealing temperatures. The presence of both COOH and C═O groups, therefore, hinders the oxygen interactions at the sheet edges at these temperatures (60−250 °C). After annealing to 200 °C, the infrared absorbance increases due to the additional carbonyl formation by about 20% in GO-5 L and ~35% in thin GO-ML, which is still less than that in bulk GO-ML films (~97%) (Figure 12). Because the sheet edges are mostly terminated with carbonyls and carboxyls in both GO-5 L and thin GO-ML samples, a strong attack of free radicals containing oxygen (originating from trapped water and oxygen species) occurs at the sheet edges, transforming carboxyls to carbonyls during thermal reduction rather than being consumed at the etch holes. It is known that radicals rapidly react with the double bond, forming an α-radical carbonyl (a carboxylate), which is relatively stable. These carboxylates can further couple with another molecule or be oxidized back to C═O. Therefore, there is much less water left around the etch holes in GO-5 L compared with that in bulk GO-ML, which results in less C═O production at the etch holes after moderate temperature anneals. The increase of the infrared absorption intensity due to additional carbonyl formation in the GO-1 L sample (~30%) is similar to that observed in the reduced thin GO-ML (~35%) sample. Although the initial carbonyl concentration of GO-1 L is less (~73 at. %) than that in the thin GO-ML (~88 at. %) sample, the larger initial total hydroxyl concentration (~17 at. %) increases the thermal reduction efficiency. As a result, there is only 3−5 at. % of oxygen remaining in the form of ethers only in reduced GO-1 L after annealing at 850 °C for 5 min.[30] In contrast, there is ~55 at. % of oxygen that remains in the reduced thin GO-ML sample having both ethers and carbonyls in the form of ketones.

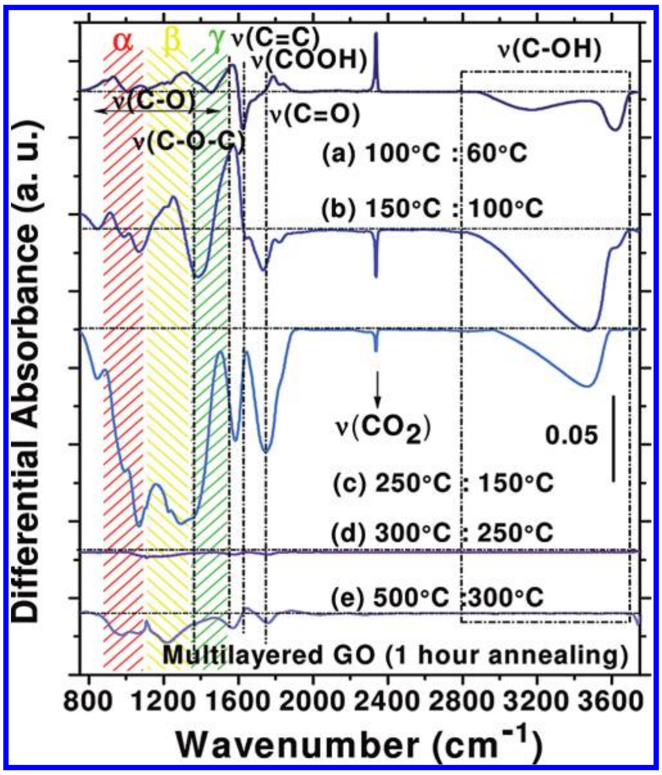

Figure 14. Transmission infrared differential spectra of multilayered GO at 60−500 °C. Changes of functional groups are shown after annealing to (a) 100−60, (b) 150−100, (c) 250−150, (d) 300−250, and (e) 500−350 °C. −(C−O−C)−, COOH, C═O, C−O, C−OH, and C═C represent epoxides, carboxyls, ketones, ethers, hydroxyls, and sp^2-hybridized C═C, respectively. The regions labeled as α, β, and γ (shown with red, yellow, and green hatched lines, respectively) include the overlapped frequencies of many functional groups (Table S5, Supporting Information).

5.3. Evidence for Defect and Vacancy Formation. On the basis of the computational study of Schniepp et al.,[40] the evolution of CO_2 resulting from defect formation into interstices during rapid heating is a possible mechanism contributing to layer exfoliation. Therefore, it is necessary to use a technique, such as in situ infrared spectroscopy, to analyze both CO_2 and CO production experimentally with regard to generation of defects during the thermal reduction process. Infrared differential spectra of the multilayered bulk GO films are shown at 60−750 °C (Figure S9, Supporting Information). A singlet peak appearing at ~2337 cm^{-1} is associated with the production of CO_2, resulting from carbon removal from the basal plane or edges, that is, defect formation. There is clearly some CO_2 formed at 75 °C, and this amount increases by a factor of 5 upon annealing to 125 °C. Above this temperature, the amount detected decreases (Figure 13). After 200 °C, trapped CO_2 is consumed.

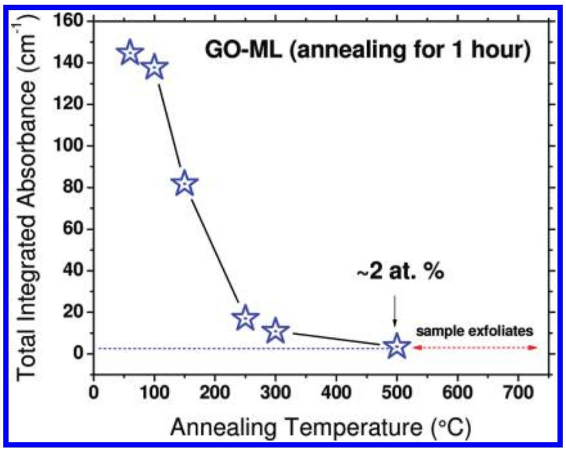

Figure 15. Total integrated infrared absorbance during thermal reduction of multilayered GO (with 33 at. % of the initial C−OH and 11 at. % of C=O concentration) for 1 h annealing at each temperature. The sample exfoliates after annealing at 500 °C so that no data points are shown for higher-temperature regimes (>500 °C).

Only epoxides start decomposing at ∼100−125 °C and are then consumed totally at ∼200 °C (Table 5). This experimental observation is supportive of some related theoretical studies in the literature. Recently, it was reported that epoxy groups on graphene relax carbon−carbon bonds underneath when aligned during the oxidation process. Epoxy decomposition, followed by the formation of ether groups, results in GO unzipping,[99] which is not mediated by hydroxyls. Such ether groups tend to align one-dimensionally, resulting in the introduction of cracks in graphite upon reduction.[100] Our experimental results show that CO production does not occur at 200 °C; therefore, CO is not produced by the decomposition of CO_2. This spectral evidence indicates that the release of CO_2 leaves behind vacancies (missing carbon atoms) and topological defects on the graphene sheets.[40]

When CO_2 production is maximum (125 °C anneal), more carbonyls are formed (Table 5). There are many plausible mechanisms predicted for this phenomenon: (1) Trapped water molecules can react with the reactive dangling bonds at the etch holes to form carbonyls. (2) Trapped water can alternatively catalyze the reaction of epoxide with heat, forming a diol that then transforms into the resonance-stabilized ketones (or carboxylates) at the etch holes. Therefore, the reactions are terminated with the formation of CO_2 at the etch holes following a radical decomposition. (3) Weak hydrogen-bond interactions between two adjacent hydroxyls can facilitate weakening of hydroxyls, resulting in a hydrogen atom migration to a neighboring hydroxyl, which then forms a carbonyl and a water molecule. There are also some other mechanisms for the formation of holes during annealing predicted by Bagri et al.,[101] which are based on the interactions between an epoxy and a hydroxyl or two epoxies or hydroxyls. (4) Migration of epoxides could be observed on the basal plane in Paci et al.'s simulations. This observation shows that some of the hole defects are likely to be terminated by carbonyls that generally exist in pairs,[102] which leads to energy stabilization.[23]

At higher annealing temperatures (>350 °C), CO is produced, as evidenced by a small singlet peak at 2115 cm^{-1}. This peak has a weak infrared absorbance that continuously increases up to 550 °C. It then decreases and disappears at 550−750 °C. The possible mechanisms are the following: (1) Backreedy et al. propose an oxidation mechanism that involves the formation of heteroatomic structures, such as semiquinones and carbonyls bound to the reactive zigzag or armchair edges, resulting in CO formation at higher temperatures.[20] Paci et al. observed such CO evolution at 1323 K with a carbon mass loss of 30% during the thermal exfoliation of GO.[103] (2) Another possible pathway is the interaction of an epoxide with a neighboring hydroxyl, which subsequently produces CO by hydrogen atom transfer at 1323 K and forms defective holes.[104] Infrared spectral qualitative analysis of the reduced multilayered bulk GO films confirms that the removal of carbonyls continues even after annealing at 650 °C (Table 5). There are still remaining carbonyl groups in the reduced GO structure after annealing at 850 °C for 5 min (Figure S6, Supporting Information, and Figure 9). To investigate further defect formation in these reduced GO films, we performed DFT simulations with a 1C-vacancy and 2C-vacancy model, involving the possible oxygen incorporation into the basal plane in the form of remaining ethers (furans or pyrans) (Table S8, Supporting Information). The simulated infrared frequencies and intensities are summarized in Table 8. The calculated frequencies show that the 1C vacancy (1122, 1159, 1296 cm^{-1}) falls in the β and γ regions with a minimal contribution at 974 cm^{-1} in the α region. However, a 2C vacancy can be spectrally observed, mainly in α and β regions (1067, 1104, 1237 cm^{-1}) with blue shifts (to the lower frequencies). The infrared differential spectra of the five- and multilayered reduced GO films (Figures S4−S6, Supporting Information) show a negative band, which is dominant in the β and γ regions with a minimal loss in the α region. This spectral evidence confirms the formation of either 1C or 2C vacancies in addition to the simultaneous removal of the carbonyls and ethers after annealing at high temperatures (250−750 °C).

5.4. Dependence on Annealing Time.

So far, we evaluated the thermal reduction process for 5 min annealing at each temperature regime. The experimental results using both infrared and ex situ X-ray photoelectron spectroscopies (XPS) show that a 5 min anneal is insufficient for complete oxygen removal even after annealing at 850 °C. A substantially longer annealing time in a furnace (5 min at 850 °C with an overall total annealing and cooling time of ∼24 h) results in a lower oxygen concentration than a direct current anneal (5 min at 850 °C with a total stepwise annealing time of ∼17 h). For reduced five-layered GO thin films, XPS spectra confirm that longer annealing times lead to lower overall oxygen concentrations (∼6 at. %), as shown in Figure S10 (Supporting Information). The remaining oxygen in reduced GO-5 L is seen in the C−O (285.5 eV) and C=O (287 eV) components in both C 1s and O 1s spectra. This indicates that a thermal anneal of five-layered GO for longer annealing times at temperatures as high as 850 °C removes most of the carbonyl groups (C=O), leaving plenty of ethers (C−O). In particular, long annealing times remove the carbonyls that had been formed due to interaction with trapped water at intermediate temperatures. These carbonyls are not removed by shorter anneal times (∼5 min) used above in the stepwise IR investigation of oxygen removal as a function of temperature. Indeed, if longer annealing times are used (1 h annealing at each specific temperature) instead of 5 min annealing, we do not observe any carbonyl formation at the intermediate steps in multilayered GO samples (Figure 14). Instead, there is a minor carbonyl formation after annealing at 100 °C with the simultaneous release of CO_2

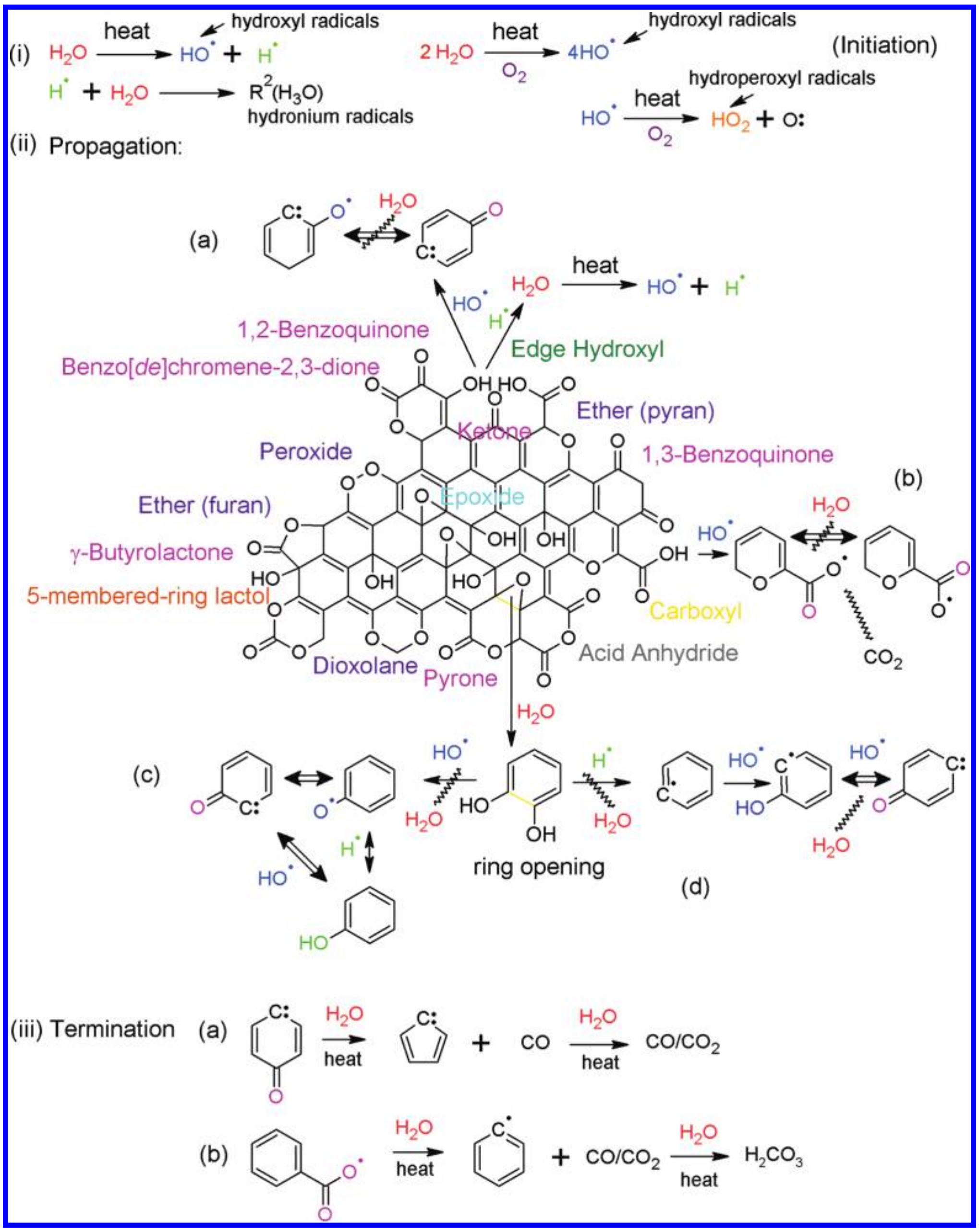

Figure 16. Schematic representations of thermal reduction mechanisms for GO reduction indicating decomposition of oxygen species through radical reactions initiating with (i) hydrolysis via combustion reactions (formation of hydroxyl, hydronium, and hydroperoxyl radicals), (ii) propagation via decarboxylation or attack on hydroxyls as well as ring-opening of epoxides, and (iii) terminating into benzyl/phenyl radicals with CO/CO_2 production.

(Figure 14, spectrum a) and further continuous dissociation of oxygen functionalities with temperature. Longer reduction times also affect the amount of remaining oxygen in reduced multilayered GO, as shown with the total integrated absorbance plot in Figure 15. This indicates that longer annealing times greatly increase the reduction efficiency, resulting in only ∼2 at. % of oxygen remaining after annealing at 500 °C, as calculated from integrated total infrared absorbance. Because the samples flake or exfoliate at higher temperatures (>500 °C), we are not able to continue the IR measurements. However, this experimental observation also confirms that the longer reduction time removes water before it can react efficiently in the interlayer and proceed to additional oxidation or to the production of several free radicals. Longer annealing times, therefore, lower the temperature necessary to remove most of the oxygen from GO.

5.5. Proposed Mechanisms for Oxygen Removal. We now propose a thermal reduction mechanism based on a selective chemistry for radical attacks either on etch holes or at the edges of GO sheets. Both the qualitative and the quantitative analyses of oxygen groups help in proposing a radical mechanism that is consistent with the experimental observations using infrared spectroscopy: (1) less carbonyl formation at the etch holes when the sheet edges are initially terminated by C═O/COOH groups because trapped hydroxyl radicals are consumed at the sheet edges (radical reactions occur preferably at the sheet edges), and (2) the amount of initial starting hydroxyl groups involving trapped water, and edge carbonyls at room temperature, determines the efficiency of the radical reactions.

Trapped water can readily initiate the heterolysis formation of hydroxyl and hydronium radicals promoted by heat as a result of combustion reactions,[105,106] which leads to production of additional radicals, such as hydroperoxyl radicals, at higher temperatures (Figure 16i). In addition, some other additional oxygen species (e.g., peroxides, hydroperoxides) generate O_2, H_2O, H_2O_2, etc. that stimulate the radical mechanism. Water molecules can either react with edge oxygen groups or catalyze the degradation of the basal plane oxygen groups with the help of hydroxyl, hydronium, or hydroperoxyl radicals (high-energy oxidants). These hydroxyl radicals and their derivatives have the capability for fostering the formation, with a high degree of the selectivity, of other hydroxyl groups.[107] Table S9 (Supporting Information) summarizes possible radical species and further radical production.

Although we cannot directly determine these radical species from infrared spectroscopy measurements, shifts in the vibrational modes can provide an indirect measure of their presence. For instance, in the presence of hydroxyl radical−water clusters, $OH(H_2O)_n$, the hydroxyl radical reduces the rate of reaction of hydroxyls due to enhanced stability of $OH(H_2O)_n$ clusters through the OH/water electron network.[108] This phenomenon result in red shifts of ∼52−78 cm^{-1} of C−OH stretch infrared frequencies, in the 3000−3700 cm^{-1} region, yielding broader bands. However, direct observation of hydroxyl radicals is quite difficult, and has not been well-described so far. A direct evidence for observing hydroxyl radicals can be either using electron spin resonance described by YanQing et al.[109] or using a probe molecule, such as terephthalate, for monitoring the radicals in water.[107] Therefore, much work has to be performed to resolve further radical issues.

A mechanism that is consistent with our experimental results involves several steps after this initiation step. The radical mechanism follows steps a−c during a propagation step with highly reactive hydroxyl radicals, as summarized in Figure 16ii. In this schematic figure, we only show the participation of hydroxyl radicals. However, the contribution of other radicals as well as oxygen species should also be considered, as summarized in Table S9 (Supporting Information). The first reaction involves the attack of the reactive hydroxyl radicals to the hydroxyl groups undergoing radical propagation and leading to the further formation of the carbonyls (Figure 16ii(a)). Carboxylates are known to decompose via decarboxylation, forming CO_2 radicals, of which unpaired electrons then migrate through the carbon framework and lead the formation of covalent bonds after finding other unpaired electrons.[110] Another reaction is, therefore, possible and involves the attack of a hydroxyl radical with a carboxyl, producing carboxylate radicals. The decomposition of carboxylates would then produce CO_2, as illustrated in Figure 16iii(b). The reactive free hydroxyl radicals are also likely to convert 1,2-diols (a ring-opening product of epoxides, keeping in mind that water catalyzes this reaction to initiate the diol formation) at the etch holes into the carbonyls (Figure 16ii(c)). All these three radical routes result in intermediate byproducts, such as formation of additional water molecules and trapped CO_2 (the latter reaction). Extra water molecules are important oxygen sources during radical reactions promoted by hydronium radicals (originally generated by water molecules) to propagate the reactions. They can then readily undergo an additional intermediate initiation and foster the oxidation reactions. There are also other oxygen radical sources (such as peroxides), which readily undergo homolysis when heated and, therefore, weaken the oxygen−oxygen bonds, producing free oxygen radicals (either hydroxyl or hydroperoxyl radicals).[106] In addition to this simple reaction mechanism initiated mainly with the hydroxyl radicals, other alternative radical species are likely to form upon annealing (Table S9, Supporting Information). At this step, in the presence of all these reactive radicals, an attack on each individual group (OH, COOH) is also expected to occur between reactive hydroxyl radicals and carboxyl and hydroxyl groups, following the two reactions, ($OH\bullet + COOH = CO_2 + H_2O\bullet$) and ($OH\bullet + OH = H_2O + H\bullet$). These radical reactions are terminated with the consumption of the hydroxyl radicals or other generated radicals, which can then further decompose in the form of trapped CO or CO_2 (Figure 16iii).

Condensation reactions can also occur at the sheet edges or on the basal plane when two oxygen groups are nearby in the presence of water catalyzing these reactions. Such reactions would produce additional water in addition to the initial amount of the trapped water in the interlayers. However, if this were the case, there would be a relatively similar carbonyl formation for all single-, three-, five- and multiple layers GO samples after moderate temperature anneals. Therefore, selective reactions of radical attacks together with cation or anion radicals are more likely to occur than condensation reactions.

In closing, we emphasize that radicals could potentially be charged, as would be the case in aqueous solutions, forming radical anions of hydroxyls.[111] Whether neutral or charged, the simple mechanism summarized in Figure 16 captures the essential multistep reactions likely to take place.

6. CONCLUSIONS

This work has examined the evolution and interactions of oxygen groups, typically randomly arranged in the material, during thermal reduction performed by 5 min annealing at each temperature. In this spectroscopic study, the spectral assignments take into account the environment and interactions of oxygen groups and quantitative information is derived from the integrated absorbance. Although complete reduction of GO films is typically not achieved in a 5 min anneal at 850 °C, the details of the reactions could be followed, thus providing information on the mechanism of thermal reduction.

The first finding, using IR spectroscopy and DFT simulations, is that GO synthesized by the modified Hummer's method is characterized by hydroxyls (possible COOH and H_2O contribution) (C−OH, 3000−3600 cm^{-1}), ketones (C═O, ∼1750−1850 cm^{-1}), carboxyls (COOH and/or H_2O) (∼1600−1750 cm^{-1}), sp^2-hybridized C═C (in-plane stretching, ∼1500−1600 cm^{-1}), and epoxides (C−O−C, ∼1280−1330 and 800−900 cm^{-1}), with all these species having weaker contributions in the 900−1500 cm^{-1} region. Second, the interactions occurring between nearby oxygen groups cause spectral shifts, characterized by variations arising from the random organization of the oxygen groups. Third, incomplete oxygen removal is observed and the degree of reduction is found to depend on the initial amount of existing carbonyl, carboxyl, and hydroxyl groups. Furthermore, the concentration of some of these groups increases upon mild anneals (∼200 °C). Fourth, the thermal reduction of GO generates defective graphene structures arising from the removal of randomly distributed oxygen groups via CO_2 or CO production, leaving the remaining oxygen in the form of very stable ethers (characterized by a sharp and strong mode at 800 cm^{-1} after an 850 °C anneal) and, in some cases, of carbonyls (e.g., in multilayered GO). We have also shown that longer annealing times (such as 1 h for each temperature) greatly reduce the amount of remaining oxygen, particularly at moderate temperatures ($\leq$600 °C).

Finally, several thermal reduction mechanisms are proposed, starting with water as an initiator that produces free radicals containing oxygen, leading to further radical reactions. These radicals then propagate by reaction with the oxygen groups of the GO films or the carbon dangling bonds at defective sites. The newly formed species after these reactions determine the amount of oxygen remaining in the reduced GO structure after annealing. These mechanisms, based on experimental support, bring a detailed overview of the whole thermal reduction process, thus providing a guide for dealing with oxygen interactions in aromatic and heterocyclic systems and for further modification or functionalization of GO as a function of annealing temperature.

■ ASSOCIATED CONTENT

Ⓢ Supporting Information. Transmission infrared absorbance spectra of single, three, and multiple layers of GO; tables summarizing the simulated infrared intensities for each oxygen functionality, the overlapped frequency regions, and spectral changes in the case of oxygen interactions; differential spectra of five- and multilayered GO; plots showing integrated infrared absorbance and normalized hydroxyl and carbonyl concentration for five- and multilayered GO; differential spectra of multilayered GO presenting CO_2 production and simulated infrared frequencies to determine the vacancies; XPS spectra of five-layered GO; differential spectra of multilayered GO summarizing 1 h annealing; and a table showing possible radical species. This material is available free of charge via the Internet at http://pubs.acs.org.

■ AUTHOR INFORMATION

Corresponding Author

*E-mail: chabal@utdallas.edu.

Present Addresses

[§]Department of Materials, Imperial College, London, U.K. SW7 2AZ.

Author Contributions

M.A. performed all IR spectroscopy work, including thermal annealing experiments, synthesis of multilayered GO, and infrared data interpretation and analysis. G.L. carried out all DFT simulations using theoretical methods. C.M. prepared 1 L, 3 L, and 5 L GO films. A.P. performed XPS measurements and XPS data interpretation with the help of R.M.W. and C.M. M. C., C.M., and A.P. reviewed the manuscript. Y.C. and K.C. supervised the IR spectroscopy work and theoretical calculations, respectively.

■ ACKNOWLEDGMENT

The authors acknowledge the partial financial support of the SWAN-NRI program, Texas Instruments (TI), and of the Department of Energy (The work of M.A. and Y.C. was fully supported by DOE-BES No. ER46657/DE-SC001951). The technical expertise of J.-F. Veyan and in-depth discussions with L. Colombo (TI), SeongYong Park, Carlo Floresca, Moon Kim E. Vogel, J. Kim, and W. Kirk at UT Dallas are also gratefully acknowledged.

■ REFERENCES

(1) Balaban, A. T.; Oniciu, D. C.; Katritzky, A. R. *Chem. Rev.* **2004**, *104*, 2777–2812.

(2) Invernale, M. A.; Acik, M.; Sotzing, G. A. Thiophene-Based Electrochromic Materials. In *Handbook of Thiophene-Based Materials: Applications in Organic Electronics and Photonics*; Perepichka, I. F., Perepichka, D. F., Eds.; John Wiley & Sons, Ltd: Chichester, U.K., 2009; Chapter 20.

(3) Ang, P. K.; Wang, S.; Bao, Q.; Thong, J. T. L.; Loh, K. P. *ACS Nano* **2009**, *3*, 3587–94.

(4) Brodie, B. C. *Philos. Trans. R. Soc. London* **1859**, *149*, 249.

(5) Staudenmaier, L. *Ber. Dtsch. Chem. Ges.* **1898**, *31*, 1481.

(6) Hummers, W. S.; Richard, J.; Offeman, E. *J. Am. Chem. Soc.* **1958**, *80*, 1339.

(7) Jeong, H.; Lee, Y. P.; Lahaye, R. J. W. E.; Park, M.; An, K. H.; Kim, I. J.; Yang, C.; Park, C. Y.; Ruoff, R. S.; Hee, Y. *J. Am. Chem. Soc.* **2008**, *130*, 1362.

(8) Hontoria-Lucas, C.; López-Peinado, A. J.; De D. López-Gónzalez, J.; Rojas-Cervantes, M. L.; Martın-Aranda, R. M. *Carbon* **1995**, *33*, 1585.

(9) Buchsteiner, A.; Lerf, A.; Pieper, J. *J. Phys. Chem. B* **2006**, *110*, 22328.

(10) Lerf, A.; He, H.; Riedl, T.; Forster, M.; Klinowski, J. *Solid State Ionics* **1997**, *101*, 857.

(11) Boukhvalov, D. W.; Katsnelson, M. I. *J. Am. Chem. Soc.* **2008**, *130*, 10697.

(12) Mermoux, M.; Chabre, Y.; Rousseau, A. *Carbon* **1991**, *29*, 469.

(13) Jeong, H. K.; Jin, M. H.; So, K. P.; Lim, S. C.; Lee, Y. H. *J. Phys. D: Appl. Phys.* **2009**, *42*, 065418.

(14) Lerf, A.; He, H.; Forster, M.; Klinowski *J. Phys. Chem. B* **1998**, *102*, 4477.

(15) Gao, W.; Alemany, L. B.; Ci, L. J.; Ajayan, P. M. *Nat. Chem.* **2009**, *1*, 403–408.

(16) Fuente, E.; Menndez, J. A.; Diez, M. A.; Montes-Morán, M. A. *J. Phys. Chem. B* **2003**, *107*, 6350.

(17) Jeong, H.-K; Noh, H.-J.; Kim, J.-Y.; Jin, M. H.; Park, C. Y.; Lee, Y. H. *Europhys. Lett.* **2008**, *82*, 67004.

(18) Nakajima, T.; Mabuchi, A.; Hagiwara, R. *Carbon* **1988**, *26*, 357.

(19) Szabó, T.; Berkesi, O.; Forgó, P.; Josepovits, K.; Sanakis, Y.; Petridis, D.; Dékány, I. *Chem. Mater.* **2006**, *18*, 2740.

(20) Backreedy, R.; Jones, J. M.; Pourkashanian, M.; Williams, A. *Faraday Discuss.* **2001**, *119*, 385.

(21) Sendt, K.; Haynes, B. S. *Proc. Combust. Inst.* **2005**, *30*, 2141.

(22) Nakamura, J.; Ito, J.; Natori, A. *J. Phys.: Conf. Ser.* **2008**, *100*, 052019.

(23) Paci, J. T.; Belytschko, T.; Schatz, G. C. *J. Phys. Chem. C* **2007**, *111*, 18099.

(24) Ruess, G. L. *Colloid J.* **1945**, *110*, 17.

(25) Fuente, E.; Menendez, J. A.; Surez, D.; Montes-Morán, M. A. *Langmuir* **2003**, *19*, 3505.

(26) Acik, M.; Mattevi, C.; Gong, C.; Lee, G.; Cho, K.; Chhowalla, M.; Chabal, Y. J. *ACS Nano* **2010**, *4*, 5861–5868.

(27) Hartono, T.; Wang, S.; Ma, Q.; Zhu, Z. *J. Colloid Interface Sci.* **2009**, *333*, 114.

(28) Park, S.; Lee, K.; Bozoklu, G.; Cai, W.; Nguyen, S. T.; Ruoff, R. S. *ACS Nano* **2008**, *2*, 572.

(29) Cassagneau, T.; Fendler, J. H. *Adv. Mater.* **1998**, *10*, 877.

(30) Acik, M.; Lee, G.; Cho, K.; Chabal, Y. J. *Nat. Mater.* **2010**, *9*, 840–845.

(31) Sendt, K.; Haynes, B. S. *Proc. Combust. Inst.* **2005**, *30*, 2141.

(32) De Boer, J. H.; van Doorn, A. B. C. *Proc. K. Ned. Akad. Wet.* **1958**, *B61*, 160.

(33) Clauss, A.; Plass, R.; Boehm, H. P.; Hofmann, U. *Z. Anorg. Allg. Chem.* **1957**, *291*, 205.

(34) Boehm, H. P. *Carbon* **1994**, *32*, 759–769.

(35) He, H.; Klinowski, J.; Forster, M.; Lerf, A. *Chem. Phys. Lett.* **1998**, *287*, 53.

(36) Cai, W.; Piner, R. D.; Stadermann, F. J.; Park, S.; Shaibat, M. A.; Ishii, Y.; Yang, D.; Velamakanni, A.; An, S. J.; Stoller, M.; An, J.; Chen, D.; Ruoff, R. S. *Science* **1998**, *321*, 815.

(37) Zhang, J.; Yang, H.; Shen, G.; Cheng, P.; Zhang, J.; Guo, S. *Chem. Commun.* **2010**, *46*, 1112–1114.

(38) Yang, D.; Velamakanni, A.; Bozoklu, G.; Park, S.; Stoller, M.; Piner, R. D.; Stankovich, S.; Jung, I.; Field, D. A.; Ventrice, C. A., Jr.; Ruoff, R. S. *Carbon* **2009**, *47*, 145.

(39) Jeong, H.; Lee, Y. P.; Jin, M. H.; Kim, E. S.; Bae, J. J.; Lee, Y. H. *Chem. Phys. Lett.* **2009**, *470*, 255.

(40) Schniepp, H. C.; Li, J.; McAllister, M. J.; Sai, H.; Herrera-Alonso, M.; Adamson, D. H.; Prud'homme, R. K.; Car, R.; Saville, D. A.; Aksay, I. A. *J. Phys. Chem. B* **2006**, *110*, 8535.

(41) Park, S.; An, J.; Jung, I.; Piner, R. D.; An, S. J.; Li, X.; Velamakanni, A.; Ruoff, R. S. *Nano Lett.* **2009**, *9*, 1593.

(42) Pretsch, E.; Bühlmann, A. C. *Structure Determination of Organic Compounds*; Springer-Verlag: Berlin, 2000.

(43) Liu, Z.; Suenaga, K.; Harris, P. J. F.; Iijima, S. *Phys. Rev. Lett.* **2009**, *102*, 15501.

(44) Boukhvalov, D. W.; Katsnelson, M. I. *J. Am. Chem. Soc.* **2008**, *130*, 10697–10701.

(45) Li, D.; Muller, M. B.; Gilje, S.; Kaner, R. B.; Wallace, G. G. *Nat. Nanotechnol.* **2008**, *3*, 101–105.

(46) Szabó, T.; Tombácz, E.; Illés, E.; Dékány, I. *Carbon* **2006**, *44*, 537–545.

(47) Su, Q.; Pang, S.; Alijani, V.; Li, C.; Feng, X.; Mullen, K. *Adv. Mater.* **2009**, *21*, 3191–3195.

(48) Hamwi, A.; Marchand, V. *J. Phys. Chem. Solids* **1996**, *57*, 867–872.

(49) Melucci, M.; Treossi, E.; Ortolani, L.; Giambastiani, G.; Morandi, V.; Klar, P.; Casiraghi, C.; Samoríae, P.; Palermo, V. *J. Mater. Chem.* **2010**, *20*, 9052–9060.

(50) Nakajima, T.; Matsuo, Y. *Carbon* **1994**, *32*, 469–475.

(51) Chen, W.; Yan, L.; Bangal, P. R. *J. Phys. Chem. C* **2010**, *114*, 19885–19890.

(52) Hou, S.; Su, S.; Kasner, M. L.; Shah, P.; Patel, K.; Madarang, C. *J. Chem. Phys. Lett.* **2010**, *501*, 68–74.

(53) Nethravathi, C.; Rajamathi, M.; Ravishankar, N.; Basit, L.; Felser, C. *Carbon* **2010**, *48*, 4343–4350.

(54) Ogoshi, T.; Ichihara, Y.; Yamagishi, T.; Nakamoto, Y. *Chem. Commun.* **2010**, *46*, 6087–6089.

(55) Shen, J.; Shi, M.; Yan, B.; Ma, H.; Li, N.; Hu, Y.; Ye, M. *Colloids Surf., B* **2010**, *81*, 434–438.

(56) Shen, J.; Shi, M.; Ma, H.; Yan, B.; Li, N.; Hu, Y.; Ye., M. *J. Colloid Interface Sci.* **2010**, *351*, 366–370.

(57) Kim, T.; Gao, Y.; Acton, O.; Yip, H.; Ma, H.; Chen, H.; Jen, A. K.-Y. *Appl. Phys. Lett.* **2010**, *97*, 023310.

(58) Meng, X.; Geng, D.; Liu, J.; Banis, M. N.; Zhang, Y.; Li, R.; Sun, X. *J. Phys. Chem. C* **2010**, *114*, 18330–18337.

(59) Sellitti, C.; Koenig, J. L.; Ishida, H. *Carbon* **1990**, *28*, 221.

(60) Yan, X.; Chen, J.; Yang, J.; Xue, Q.; Miele, P. *ACS Appl. Mater. Interfaces* **2010**, *2*, 2521–2529.

(61) Chandra, V.; Park, J.; Chun, Y.; Lee, J. W.; Hwang, I.; Kim, K. S. *ACS Nano* **2010**, *4*, 3979–3986.

(62) Lee, D. W.; Santos, V.; De Los, L.; Seo, J. W.; Felix, L. L.; Bustamante, A. D.; Cole, J. M.; Barnes, C. H. W. *J. Phys. Chem. B* **2010**, *114*, 5723–5728.

(63) Xu, J.; Wang, K.; Zu, S.; Han, B.; Wei, Z. *ACS Nano* **2010**, *4*, 5019–5026.

(64) Oh, J.; Lee, J.; Koo, J. C.; Choi, H. R.; Lee, Y.; Kim, T.; Luong, N. D.; Nam, J. *J. Mater. Chem.* **2010**, *20*, 9200–9204.

(65) Zhang, S.; Song, H.; Guo, P.; Zhou, J.; Chen, X. *Carbon* **2010**, *48*, 4197–4214.

(66) Gonçalves, G.; Marques, P. A. A. P.; Barros-Timmons, A.; Bdkin, I.; Singh, M. K.; Emami, N.; Grácio, J. *J. Mater. Chem.* **2010**, *20*, 9927–9934.

(67) Bon, S. B.; Valentini, L.; Kenny, J. M. *Chem. Phys. Lett.* **2010**, *494*, 264–268.

(68) Pham, T. A.; Kumar, N. A.; Jeong, Y. T. *Synth. Met.* **2010**, *160*, 2028–2036.

(69) Karousis, N.; Sandanayaka, A. S. D.; Hasobe, T.; Economopoulos, S. P.; Sarantopouloua, E.; Tagmatarchis, N. *J. Mater. Chem.* **2011**, *21*, 109–117.

(70) Hontoria-Lucas, C.; López-Peinado, A. J.; De D. López-González, J.; Rojas-Cervantes, M. L.; Martín-Aranda, R. M. *Carbon* **1995**, *33*, 1585–1592.

(71) Wu, X.; Sprinkle, M.; Li, X.; Ming, F.; Berger, C.; de Heer, W. A. *Phys. Rev. Lett.* **2008**, *101*, 026801.

(72) Jung, I.; Dikin, D. A.; Piner, R. D.; Ruoff, R. S. *Nano Lett.* **2008**, *8*, 4283–7.

(73) Papirer, E.; Dentzer, J.; Li, S.; Donnet, J. B. *Carbon* **1991**, *29*, 69.

(74) Gao, X.; Jang, J.; Nagase, S. *J. Phys. Chem. C* **2010**, *114*, 832–842.

(75) Xu, K.; Ye, P. D. *J. Phys. Chem. C* **2010**, *114*, 10505–10511.

(76) Zhou, X.; Wei, Y.; He, Q.; Boey, F.; Zhanga, Q.; Zhang, H. *Chem. Commun.* **2010**, *46*, 6974–6976.

(77) Wojcik, A.; Kamat, P. V. *ACS Nano* **2010**, *4*, 6697–6706.

(78) Yorimitsu, H.; Nakamura, T.; Shinokubo, H.; Oshima, K.; Omoto, K.; Fujimoto, H. *J. Am. Chem. Soc.* **2000**, *122*, 11041–1104.

(79) Maruyama, S.; Kojima, R.; Miyauchi, Y.; Chiashi, S.; Kohno, M. *Chem. Phys. Lett.* **2002**, *360*, 229–234.

(80) Ohkita, K.; Tsubokowa, N.; Saitoh, E.; Noda, M.; Takashima, N. *Carbon* **1975**, *13*, 443.

(81) Lenher, S. *J. Am. Chem. Soc.* **1931**, *53*, 3752.

(82) Menendez, J. A.; Radovic, L. R.; Xia, B.; Phillips, J. *J. Phys. Chem.* **1996**, *100*, 17243–17248.

(83) Phillips, J.; Kelly, D. J.; Radovic, D. L.; Xie, D. F. *J. Phys. Chem. B* **2000**, *104*, 8170–8176.

(84) Dean, V. W.; Frenklach, M.; Phillips, J. *J. Phys. Chem.* **1988**, *92*, 5731–5738.

(85) Slabaugh, W. H.; Seiler, B. C. *J. Phys. Chem.* **1962**, *66*, 396.

(86) Jung, I.; Field, D. A.; Clark, N. J.; Zhu, Y.; Yang, D.; Piner, R. D.; Stankovich, S.; Dikin, D. A.; Geisler, H.; Ventrice, C. A., Jr.; Ruoff, R. S. *J. Phys. Chem. C* **2009**, *113*, 18480–18486.

(87) Wei, Z.; Wang, D.; Kim, S.; Kim, S.; Hu, Y.; Yakes, M. K.; Laracuente, A. R.; Dai, Z.; Marder, S. R.; Berger, C.; King, W. P.; de Heer, W. A.; Sheehan, P. E.; Riedo, E. *Science* **2010**, *328*, 1373.

(88) Backreedy, R.; Jones, J. M.; Pourkashanian, M.; Williams, A. *Faraday Discuss.* **2001**, *119*, 385–394.

(89) Hummers, W. S.; Richard, J.; Offeman, E. *J. Am. Chem. Soc.* **1958**, *80*, 1339.

(90) Gilje, S.; Han, S.; Wang, M.; Wang, K. L.; Kaner, R. B. *Nano Lett.* **2007**, *7*, 3394.

(91) Goki, E.; Giovanni, F.; Chhowalla, M. *Nat. Nanotechnol.* **2008**, *3*, 270.

(92) Mkhoyan, K. A.; Contryman, A. W.; Silcox, J.; Stewart, D. A.; Eda, G.; Mattevi, C.; Miller, S.; Chhowalla, M. *Nano Lett.* **2009**, *9*, 1058–1063.

(93) Kresse, G.; Furthemuller, J. *Comput. Mater. Sci.* **1996**, *6*, 15–50.

(94) Blochl, P. *Phys. Rev. B: Condens. Matter Mater. Phys.* **1994**, *50*, 17953–79.

(95) Yukhnovskii, I. N. *Theor. Exp. Chem.* **1967**, *3*, 67.

(96) Jeong, H.; Lee, Y. P.; Lahaye, R. J. W. E.; Park, M.; An, K. H.; Kim, Yang, C.; Park, C. Y.; Ruoff, R. S.; Lee, Y. H. *J. Am. Chem. Soc.* **2008**, *130*, 1362–1366.

(97) Hadzi, D.; Novak, A. *Trans. Faraday Soc.* **1955**, *51*, 1614.

(98) Szabó, T.; Berkesi, O.; Dékány, I. *Carbon* **2005**, *43*, 3181–3194.

(99) Li, J.-L.; Kudin, K. N.; McAllister, M. J.; Prud'homme, R. K.; Aksay, I. A.; Car, R. *Phys. Rev. Lett.* **2006**, *96*, 176101.

(100) Bourlinos, A. B.; Gournis, D.; Petridis, D.; Szabó, T.; Szeri, A.; Dékány, I. *Langmuir* **2003**, *19*, 6050.

(101) Bagri, A.; Grantab, R.; Medhekar, N. V.; Shenoy, V. B. *J. Phys. Chem. C* **2010**, *114*, 12053–12061.

(102) Li, Z.; Zhang, W.; Luo, Y.; Yang, J.; Huo, J. G. *J. Am. Chem. Soc.* **2009**, *131*, 6320.

(103) Moulijn, J. A.; Kapteijn, F. *Carbon* **1995**, *33*, 1155.

(104) Li, X.; Wang, X.; Zhang, L.; Lee, S.; Dai, H. *Science* **2008**, *319*, 1229.

(105) Gray, P. *Trans. Faraday Soc.* **1959**, *55*, 408–417.

(106) Frost, G. J.; Ellison, G. B.; Vaida, V. *J. Phys. Chem. A* **1999**, *103*, 10169–10178.

(107) Page, S. E.; Arnold, W. A.; McNeill, K. *J. Environ. Monit.* **2010**, *12*, 1658–1665.

(108) Allodi, M. A.; Dunn, M. E.; Livada, J.; Kirschner, K. N.; Shields, G. C. *J. Phys. Chem. A* **2006**, *110*, 13283–13289.

(109) YanQing, C.; ZuCheng, W.; YuQiong, L. *Chin. Sci. Bull.* **2007**, *52*, 1432–1435.

(110) An, S. J.; Zhu, Y.; Lee, S. H.; Stoller, M. D.; Emilsson, T.; Ark, S.; Velamakanni, A.; An, J.; Ruoff, R. S. *J. Phys. Chem. Lett.* **2010**, *1*, 1259–1263.

(111) Sehested, K.; Holcman, J. *J. Phys. Chem.* **1978**, *82*, 651–653.